PERGAMON

Deep-Sea Research II 47 (2000) 1353–1385

DEEP-SEA RESEARCH
PART II

The Northeast Monsoon's impact on mixing, phytoplankton biomass and nutrient cycling in the Arabian Sea

J.D. Wiggert[a,*], B.H. Jones[b], T.D. Dickey[c], K.H. Brink[d], R.A. Weller[d], J. Marra[e], L.A. Codispoti[f]

[a]*University of Maryland, Earth System Science, Interdisciplinary Center, CSS-2207, College Park, MD 20742-2465, USA*
[b]*Department of Biological Sciences, University of Southern California, Los Angeles, CA, 90089-0371, USA*
[c]*ICESS, UC Santa Barbara, Santa Barbara, CA, 93106-3060, USA*
[d]*Woods Hole Oceanographic Institution, Woods Hole, MA, 02543, USA*
[e]*Lamont-Doherty Earth Observatory, Palisades, NY, 10964, USA*
[f]*CCPO, Old Dominion University, Norfolk, VA, 23529, USA*

Received 29 April 1998; received in revised form 7 June 1999; accepted 10 June 1999

Abstract

In the northern Arabian Sea, atmospheric conditions during the Northeast (winter) Monsoon lead to deep convective mixing. Due to the proximity of the permanent pycnocline to the sea surface, this mixing does not penetrate below 125 m. However, a strong nitracline is also present and the deep convection results in significant nitrate flux into the surface waters. This leads to nitrate concentrations over the upper 100 m that exceed 4 μM toward the end of the monsoon. During the 1994/1995 US JGOFS/Arabian Sea expedition, the mean areal gross primary production over two successive Northeast Monsoons was determined to be 1.35 $gC/m^2/d$. Thus, despite the deep penetrative convection, high rates of primary productivity were maintained. An interdisciplinary model was developed to elucidate the biogeochemical processes involved in supporting the elevated productivity. This model consisted of a 1-D mixed-layer model coupled to a set of equations that tracked phytoplankton growth and the concentration of the two major nutrients (nitrate and ammonium). Zooplankton grazing was parameterized by a rate constant determined by shipboard experiments. Model boundary conditions consist of meteorological time-series measured from the surface buoy that was part of the ONR Arabian Sea Experiment's central mooring. Our numerical experiments show that elevated surface evaporation, and the associated salinization of the mixed layer, strongly contributes to the

* Corresponding author. Tel.: 001-301-405-4971; fax: 001-301-405-8468.
E-mail address: jwiggert@neptune.gsfc.nasa.gov (J.D. Wiggert).

0967-0645/00/$ - see front matter
PII: S0967-0645(99)00147-2

frequency and penetration depth of the observed convective mixing. Cooler surface temperatures, increased nitrate entrainment, reduced water column stratification, and lower near-surface chlorophyll *a* concentrations all result from this enhanced mixing. The model also captured a dependence on regenerated nitrogen observed in nutrient uptake experiments performed during the Northeast Monsoon. Our numerical experiments also indicate that variability in mean pycnocline depth causes up to a 25% reduction in areal chlorophyll *a* concentration. We hypothesize that such shifts in pycnocline depth may contribute to the interannual variations in primary production and surface chlorophyll *a* concentration that have been previously observed in this region.

1. Introduction

The recent US JGOFS Arabian Sea Process Study and ONR Forced Upper Ocean Dynamics Program brought together an extensive array of investigations designed to observe the physical and biogeochemical processes that occur in this region (Smith et al., 1998). Within a relatively small ocean basin, the Arabian Sea's ecosystem ranges from eutrophic through oligotrophic, including extensive wind-driven upwelling that results in a 'nutrient trap' that contributes to the extensive subsurface oxygen minimum zone (Ryther et al., 1966; Burkill et al., 1993; Warren, 1994; Morrison et al., 1998). This range of biogeochemical provinces is due largely to extreme meteorological forcing, termed the monsoon, which manifests itself as strong, seasonally reversing winds. The two components of this annual cycle are typically referred to as the Southwest (summer) and Northeast (winter) Monsoons (SWM and NEM, respectively). Within the lower troposphere, these represent warm, moist air leaving eastern Africa roughly parallel to the Somalia coastline, and relatively cool, dry air emanating from the high-pressure region behind the Tibetan Plateau, respectively (Findlater, 1969; Tomczak and Godfrey, 1994).

Both components of the monsoon drive the mixing and transport that determine upper ocean structure. However, the specific forcing mechanisms differ. During the summer, upper-ocean structure is set by extremely high surface wind stress ($|\bar{\tau}| = 0.22\ \mathrm{N/m^2}$) and horizontal advection of upwelled coastal waters originating along the Arabian Peninsula. During the winter, upper-ocean structure is set by moderate wind forcing ($|\bar{\tau}| = 0.07\ \mathrm{N/m^2}$) and deep, penetrative convection due to a negative net heat flux (Q_{NET}). This occurs despite significant levels of insolation (Q_{SW}) consistent with summertime values. The components responsible for negative Q_{NET} are latent (Q_{LA}) and net long-wave (Q_{LW}) heat flux that result from the low relative humidity (RH = 70.3%) and air temperatures that are almost 1°C lower than sea-surface temperatures (Weller et al., 1998). The low RH also drives evaporation that elevates surface salinity. Wintertime evaporation accounts for around 60% of the net E–P (i.e., evaporation – precipitation) of 1000 mm/yr reported in climatologies of the northern Arabian Sea (Tomczak and Godfrey, 1994). The two monsoon mixing regimes produce a pronounced bimodal character in seasonal mixed layer depth

(Z_{ML}), with the deepest excursions (100–120 m (NEM); and 70–80 m (SWM)) occurring during the peak of each monsoon component (Dickey et al., 1998).

Phytoplankton biomass concentrations and primary productivity rates from the northern Arabian Sea are relatively high during both monsoons (Marra et al., 1998). Values of primary production determined during the SWM (1.50 $gC/m^2/d$ (Barber et al., 2000) correspond well to previous measurements within the region (Kabanova, 1968; Bauer et al., 1991). Values of primary production determined during the 1994 and 1995 NEM (1.64 and 1.06 $gC/m^2/d$, (Barber et al., 2000) were up to five times higher than most previously reported values (Kabanova, 1968; Banse, 1987; Bauer et al., 1991). However, values consistent with these recent measurements also have been reported (Ryther et al., 1966; Madhupratap et al., 1996). Additionally, significant interannual variability has been noted in surface biomass concentrations (Banse, 1987; Bauer et al., 1991), and a range of 5–6 fold may be seen around the mooring site (15°30′N, 61°30′E) within January–February composites of the historical ocean color imagery (CZCS, from 1979–1985, see http://seawifs.gsfc.nasa.gov). A multi-year particle flux study in the same region as the present experiment's moored array generally reveals a bimodal character in annual flux rate (Nair et al., 1989), reminiscent of the annual Z_{ML} cycle. The flux maxima coincide with the height of each monsoon, but the NEM peak exhibits significant interannual variation (Haake et al., 1993), consistent with the surface biomass observations and primary productivity measurements discussed previously.

The region's hydrographic structure may be responsible for this interannual variability. The principal hydrographic difference between this region and other oceanic regions undergoing wintertime convection and the associated transport of nitrate into surface waters is the near surface presence of the permanent thermocline (Ryther et al., 1966). In other regions (e.g., the Sargasso Sea), wintertime convection typically results in a Z_{ML} of 150–250 m (Michaels et al., 1994). This does not permit a daily dose of photosynthetically available radiation (PAR) capable of sustaining significant primary productivity. Therefore, phytoplankton concentrations, if measurable, are extremely low (Dickey et al., 1993; Wiggert, 1995). Under these conditions, net primary production becomes positive only with the onset of seasonal stratification and the mixed layer's rise above the compensation depth.

In summary, the northern Arabian Sea exhibits a number of physical and biogeochemical responses to monsoonal atmospheric forcing. We are particularly interested in how biogeochemical processes respond to the convective mixing of the NEM. In this study, we focus on the role that wintertime evaporation plays in defining phytoplankton and inorganic nutrient variability (specifically nitrate (NO_3) and ammonium (NH_4)). Primary production principally derived from one of these nutrient pools has been classified as either 'new' (NO_3) or 'regenerated' (NH_4) (Dugdale and Goering, 1967). The *f*-ratio, reported within the modeling results, is the ratio of new production to total production. This parameter is used to quantify spatially and temporally the dominant phytoplankton nutrient source, and is of interest within the present context since the in situ observations reveal low *f*-ratios and elevated rates of primary productivity despite persistently elevated nitrate concentrations (McCarthy et al., 1999).

An interdisciplinary model was developed to study the observed nutrient dynamics of the NEM and how this supports the (surprisingly) high levels of primary productivity. Literature sources suggest that this region historically has been subject to significant interannual variability in both surface phytoplankton concentration and rates of primary productivity. The interdisciplinary model has been extended to explore a possible mechanism for generating this variability. This paper presents observations that illustrate the cumulative effect of the NEM at the mooring site, discusses the development and application of the interdisciplinary model, and presents model simulations for four case studies.

2. Observations: The physical and biogeochemical setting

The observations presented and utilized here consist of spatial mapping of physical and biogeochemical properties from hydrographic and SeaSoar cruises and oceanic and meteorological time series from a moored-instrument array. The broad array of instrumentation and measurement techniques has been fully documented elsewhere, and is briefly presented here with appropriate references for the interested reader. An overview of the US portion of the recent Arabian Sea Expedition, during which these measurements were made, was presented by (Smith et al., 1998). Hydrographic data pertinent to this investigation consist of nutrient concentrations obtained from CTD casts taken during the process cruises (Morrison et al., 1998). Nutrient uptake experiments that characterized rates of new versus regenerated primary production also were performed on the NEM process cruises (McCarthy et al., 1999). The SeaSoar is a towed undulating instrument platform that nominally cycles between 5 and 300 m every 12 min, measuring a full suite of physical and biogeochemical parameters (Brink et al., 1998) along the cruise track (Fig. 1). The moored instrument array consisted of a surface buoy outfitted with meteorological sensors that measured heat and momentum fluxes at the air-sea interface and subsurface instruments that measured physical and bio-optical properties of the upper ocean (Dickey et al., 1998; Marra et al., 1998; Weller et al., 1998). This mooring was located in the center of the bowtie-shaped portion of the SeaSoar cruise track (15.5°N, 61.5°E, Fig. 1).

Quasi-synoptic spatial measurements from the first two SeaSoar cruises (TN042 and TN044) and hydrographic observations from the intervening process cruise (TN043) are used to characterize the regional impact of the NEM (see Table 1 for cruise dates). The SeaSoar measurements shown here were taken from the bowtie-shaped cruise track that traversed the moored array (Fig. 1). The timing of the three cruises (Table 1) is also depicted on a temperature time-series from the central mooring (Fig. 2). As defined by the meteorological conditions (Weller et al., 1998), TN042 coincided with the onset of the NEM, TN043 occurred during the height of the NEM, and TN044 took place during the transition from the NEM to the spring intermonsoon. We present salinity, temperature and chlorophyll *a* from these two SeaSoar cruises to illustrate the NEM's cumulative effect on physical and bio-optical properties of the surface waters. SeaSoar-based chlorophyll *a* was determined from the in situ measurements of stimulated fluorescence using a chlorophyll calibration

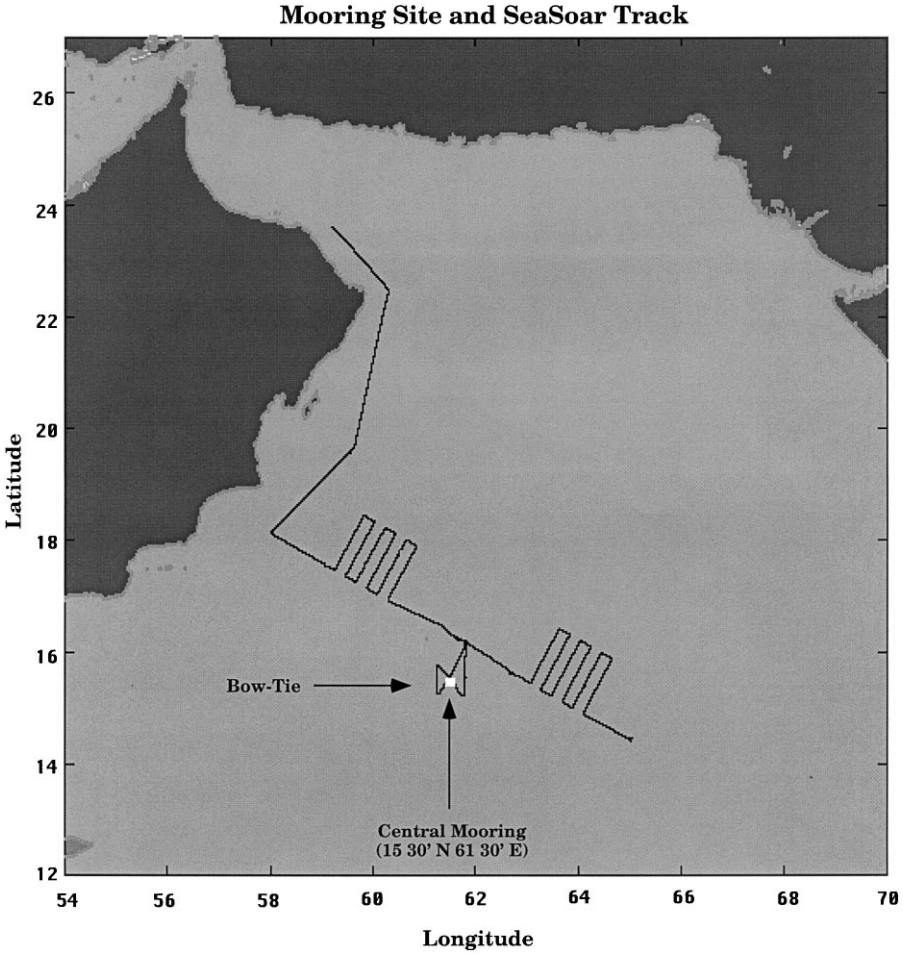

Fig. 1. Experiment Site. The full cruise track for the first Arabian Sea seasoar cruise is shown. The mooring site and the bowtie-shaped cruise track around the moored array are indicated.

based on a time-series of onboard chlorophyll extractions performed on surface water samples (Yentsch and Phinney, pers. comm., 1997). Data from the southern line of TN043 reveal the nutrient distribution from the Omani coast to the central Arabian Sea and encompass a wide range (eutrophic through oligotrophic) of pelagic environments (Morrison et al., 1998).

Over the course of the NEM, SeaSoar-measured temperature and salinity indicate: (1) a deepening of the surface mixed layer from 50 to 110 m; (2) a 3% increase in salinity at the base of the mixed layer; and (3) a significant weakening of thermal stratification within the upper 300 m (Figs. 3 and 4). Despite this erosion of the seasonal thermocline, a significant gradient ($\Delta T \approx 4^{\circ}$C) between 120 and 150 m

Table 1
Summary of cruise designations, dates[a] and descriptions

Cruise #	Calendar dates	Julian day	Cruise type	Monsoon condition
TN042	28 Nov.–19 Dec. 1994	332–353	SeaSoar Cruise #1	Early NE Monsoon
TN043	8 Jan.–5 Feb. 1995	8–36	Process Cruise #1	NE Monsoon
TN044	9 Feb.–3 Mar. 1995	40–62	SeaSoar Cruise #2	Spring Intermonsoon

[a]Cruise dates following those listed in (Smith et al., 1998). Julian day is provided to reinforce the relative timing between cruise periods, moored time-series and model domain as depicted in Fig. 2. Monsoon condition is based on meteorological measurements obtained by the surface buoy of the central mooring (Weller et al., 1998).

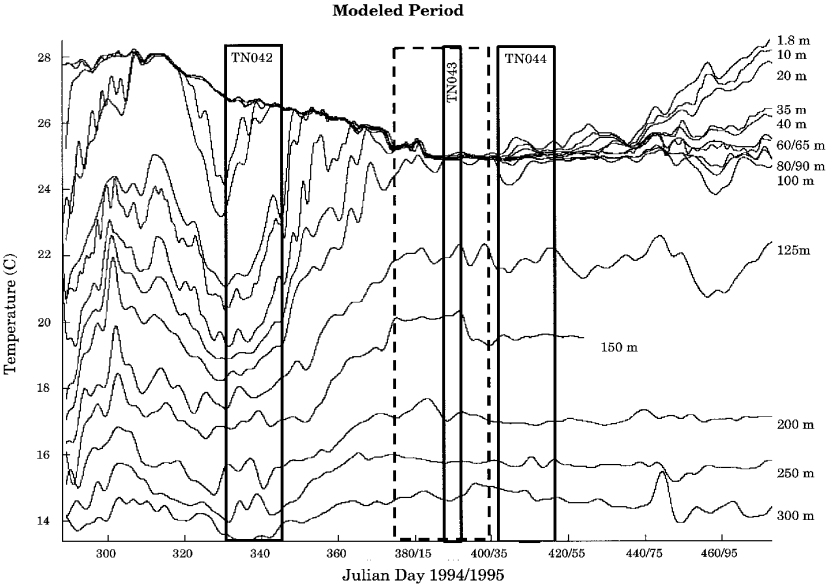

Fig. 2. Stacked temperature time-series. These data were obtained by moored MVMS packages, SeaCats and TPODS. The depths for each time-series are indicated. The two week period around each SeaSoar cruise's traverse of the moored array (TN042 and TN044) and the period of the first process cruise (TN043) are indicated by the solid boxes. The dashed-line box depicts the time domain chosen for the modeling experiments. The time line has been given in Julian Day for both 1994 and 1995 when applicable.

remains by the end of the NEM. This traps the salt produced by the NEM's evaporative conditions within the surface layer, and the resulting salinity inversion indicates that the water column should experience salt fingering (Ruddick, 1997). Air temperatures that were generally 1°C cooler than sea surface temperatures as well as the diurnal cycle associated with Q_{SW} provide additional mixing impetus. These mixing tendencies combine to produce the consistent diurnal oscillation observed in mixed-layer depth time-series. Here, we define mixed-layer depth (Z_{ML}) as the depth at

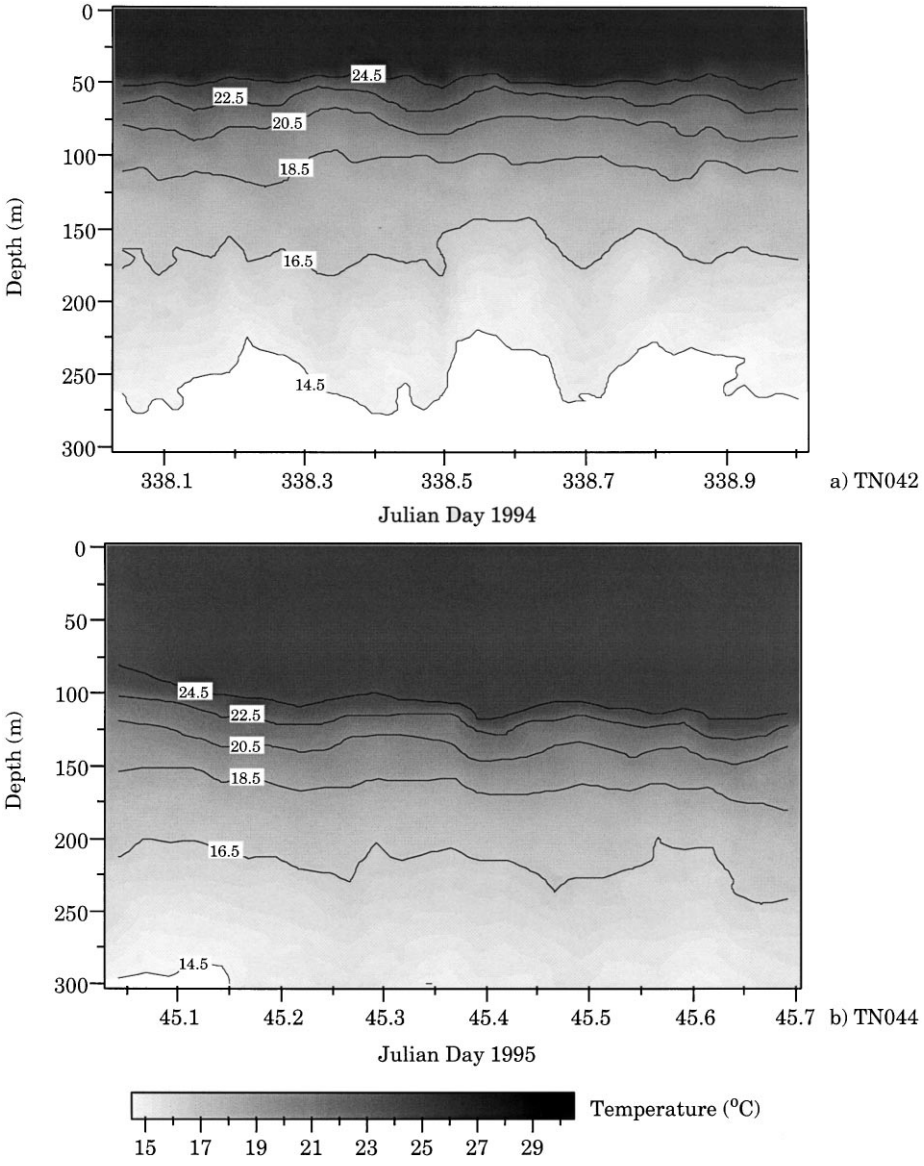

Fig. 3. Temperature around the moored array during (a) TN042 and (b) TN044. These reveal the cumulative effect of NEM forcing in the region. The gray scale used for both temperature distributions is consistent. Typically, the SeaSoar took 24 h to complete its circuit around the moorings. The data have been presented as a function of fractional Julian Day along the abscissa. The calendar day for each traverse is 4 December 1994 and 14 February 1995. The entire sampling pattern around the moorings was not completed during TN044 due to difficulties with the SeaSoar's flight characteristics, resulting in the shortened time period in the TN044 distributions.

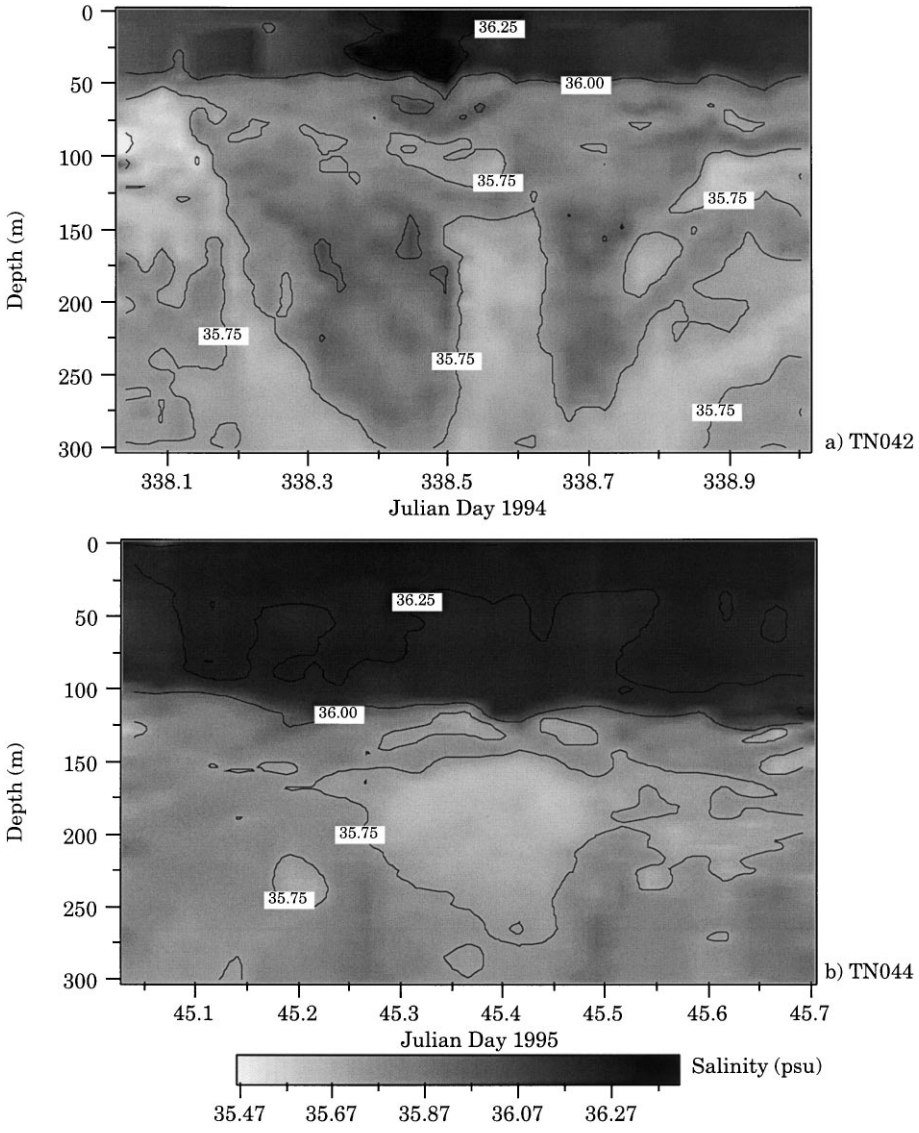

Fig. 4. Salinity around the moored array during (a) TN042 and (b) TN044. These reveal the salinization of the mixed layer that occurred over the course of the NEM. The gray scale used for both salinity distributions is consistent. Sub-mixed layer salinity features appear during both cruises. These have corresponding thermal signatures and indicate significant water mass interleaving in the region.

which a difference (ΔT) from the observed surface temperatures is reached. Based on a ΔT of 0.1°C, Z_{ML} ranged from 10–15 m during the day and 105 m at night (Fig. 5a). Furthermore, Z_{ML} defined with a more liberal ΔT of 0.5°C reveals diurnal penetration that less consistently reached 130 m (not shown).

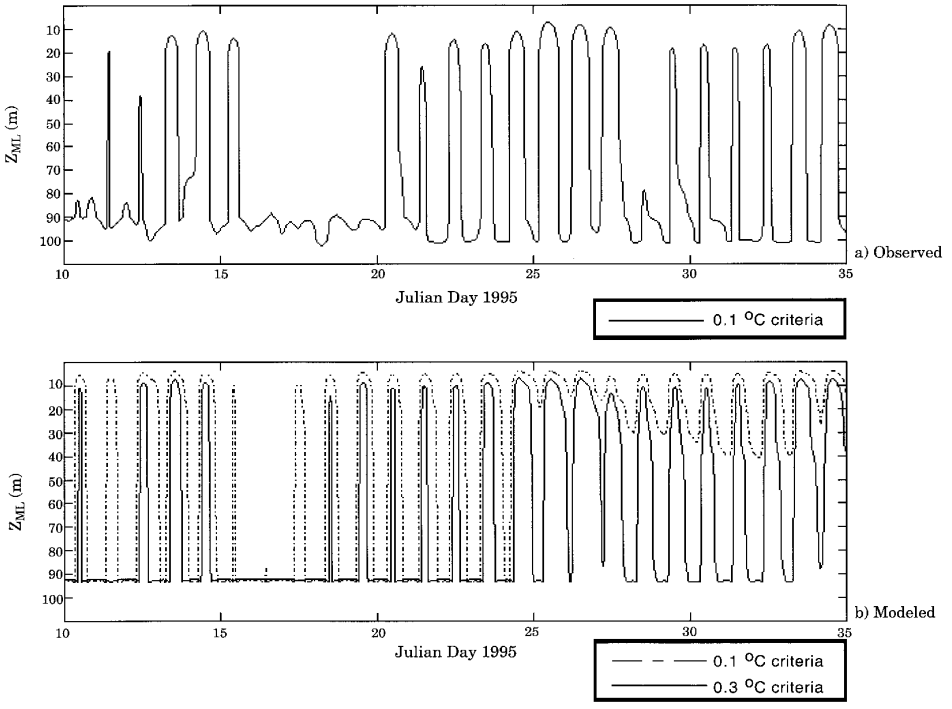

Fig. 5. Intercomparison of mixed layer (Z_{ML}) time-series. (a) Time-series of Z_{ML} determined from the moored temperature time-series (Fig. 2). The Z_{ML} criterion was a 0.1°C difference in temperature from the sea surface. The diurnal shoaling and deepening of the mixed layer between 10 and 100 m is evident. The extent of the time-series corresponds to the period chosen for the model runs. (b) Time-series of Z_{ML} determined using temperature from Case I model result. Two temperature criteria are represented here in order to expand on the model's ability to emulate the observations. The dashed line represents the 0.1°C condition while the solid line represents the 0.3°C condition.

These hydrodynamic conditions have significant implications with respect to the vertical distribution and redistribution of the local biogeochemical fields. During TN043, nitrate concentration was greater than 1 μM at the surface, at least 4 μM at 60 m and 15–25 μM at 125 m, over the entire southern line (Fig. 6a). This sub-mixed-layer nitrate reservoir is easily accessible by the noted convective mixing, and the strong gradient over the upper 100 m indicates that a significant transfer of nitrate into the euphotic zone took place. Additionally, ammonium was produced within the mixed layer (Fig. 6b), where concentrations of at least 0.2 μM were observed in the vicinity of the central mooring, 650 km offshore. Phytoplankton biomass is shown in the two chlorophyll *a* distributions measured by the SeaSoar (Fig. 7). Chl *a* concentration within the upper 50 m during TN044 is 2.5 times higher than the concentration observed during TN042. A modest increase in Chl *a* between 50 and 100 m is also

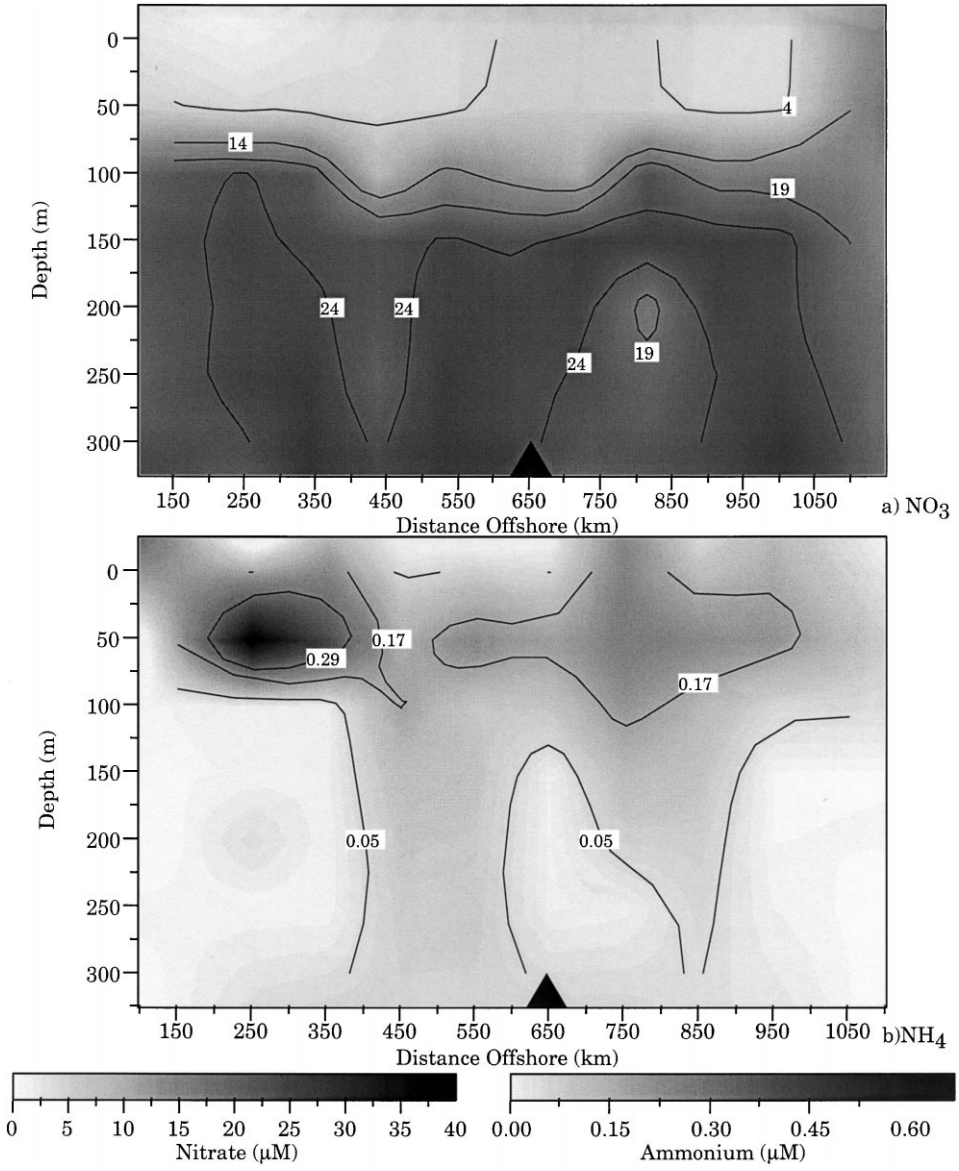

Fig. 6. (a) Nitrate and (b) ammonium concentration (μM) along the southern (JGOFS) line during the first process cruise (TN043). The nitrate map reveals elevated concentrations within the mixed layer (~ 4 μM) and concentrations ranging up to 30 μM within 100 m of the mixed layer's base. The ammonium map reveals concentrations up to 0.3 μM within the mixed layer and $\leqslant 0.5$ μM at depth near the mooring. The abscissa gives distance offshore (km). The central mooring is 650 km offshore (marked by the solid triangle) and offset about 50 km from the southern line. The southern line corresponds to the main offshore line incorporated within the seasoar track (Fig. 1).

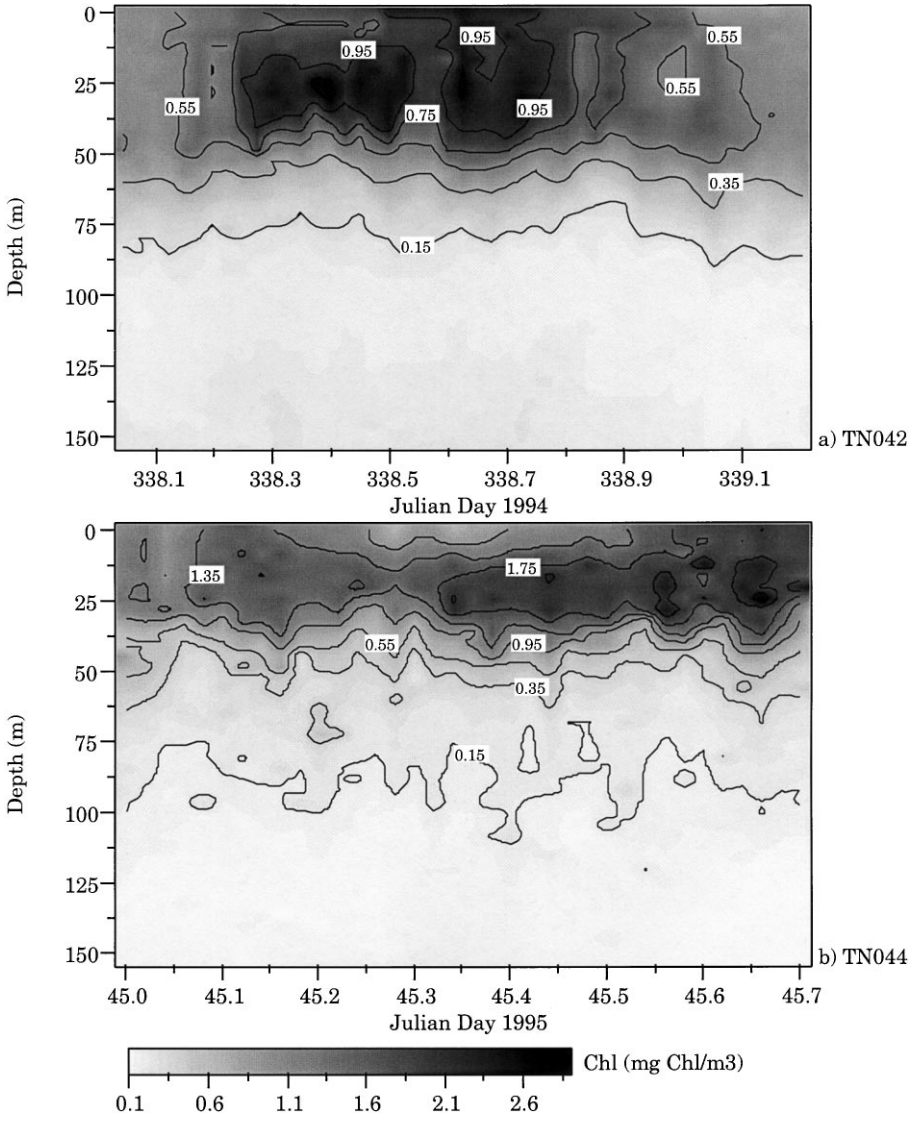

Fig. 7. Chl *a* around the moored array during (a) TN042 and (b) TN044. Note that the gray scale for these two Chl *a* distributions is not consistent. These maps indicate an increase in Chl *a* over the entire euphotic zone by the end of the NEM. Surface concentrations during TN044 are 2–3 times greater than during TN042. The Chl *a* distribution from TN044 also reveals higher concentrations at depth, indicative of the mixing associated with NEM forcing.

indicated during TN044, and the depth of the 0.15 mg Chl a/m^3 isopleth shows more vertical variability and extends to 100 m in several instances, whereas during TN042 it is consistently above 80 m.

Table 2
Constant terms used within the nutrient cycling equation set. These are based on in-situ measurements from the first Arabian Sea process cruise (TN043), literature values or sensitivity analyses (SA) performed during this investigation

Description	Symbol	Units	Value	Source
Chl specific absorption	a_{chl}	m^2/g Chl *a*	11.1	TN043; Marra
Max. quantum yield	ϕ_m	molC/Ein	0.06	TN043; Marra
Min. C : Chl	Θ_m	molC/g Chl *a*	2.00	Kiefer, 1993
Max. growth rate (N_a)	p_{max}	d^{-1}	1.30	TN043; Goericke
NO_3 uptake inhibition	Ψ	m^3/mMol N	9.75	TN043; McCarthy
$\frac{1}{2}$ Saturation constant (N_n)	κ_1	mMol N/m^3	0.50	Wiggert, 1995
$\frac{1}{2}$ Saturation constant (N_r)	κ_2	mMol N/m^3	0.10	Wiggert, 1995
Grazing efficiency (%)	π_1	%	0.50	SA
Phytoplankton losses (death and cell lysis)	r_1	d^{-1}	0.01	SA
Zooplankton grazing	z_1	d^{-1}	0.28	TN043; Caron
Empirical constant	b_Θ	—	15.00	Kiefer, 1993

3. Methods: The interdisciplinary model

3.1. Formulation

A set of equations that track nitrogen flow between phytoplankton and two nutrient pools has been coupled to a 1-D mixed layer model to study nutrient utilization during the NEM within the northern Arabian Sea. The physical model is the level 2.5 Mellor–Yamada second moment turbulence closure scheme. The equations governing the mean quantities are listed below (Eqs. (1.1)–(1.4)). Predictive equations for turbulent quantities (e.g., turbulent length scale and turbulent kinetic energy), used to predict turbulent diffusivities of heat (K_H) and momentum (K_M), are part of the full model equation set and have been fully documented elsewhere (Mellor and Yamada, 1982). Details of the specific coupling between the physical and biological components of the model are based on, and consistent with, previous interdisciplinary modeling studies of the Sargasso Sea (Wiggert, 1995). Briefly, this consists of the redistribution of the biogeochemical fields by turbulent diffusion (K_H) and the inclusion of the penetrating component of short wave radiation in the heat equation (second term on RHS of Eq. (1.3)), which has both a visible (I_0) and infrared (I_{IR}) component. Vertical attenuation of I_0 (i.e., PAR) provides a mechanism for feedback from the vertical biomass distribution to thermal structure via biomass-specific, diffuse attenuation of irradiance (Eq. (2.1)).

The biogeochemical components included here were limited to one class of phytoplankton (N_a) and the two major nutrients, nitrate (N_n) and ammonium (N_r) (Eqs. (1.5)–(1.7)). The evolution of phytoplankton concentration in this formulation consists of photosynthetic growth, zooplankton grazing, vertical mixing via turbulent diffusion, and losses of phytoplankton biomass due to cell death and lysis (Eq. (1.5)). The zooplankton grazing rate (z_1) applied here was determined by in situ experiments

performed during TN043 (Caron and Dennett, 2000). Its value is listed, along with additional pertinent modeling parameters, in Table 2. The grazing term serves to close the equation set and provides a simple formulation for nutrient cycling. A portion of the grazing term ($\pi_1 z_1$) is reintroduced into the system as ammonium (Eq. (1.7)) and represents a zooplankton feeding efficiency. The noted losses of phytoplankton biomass are also reintroduced via the ammonium equation (r_1). Vertical redistribution of all physical and biogeochemical constituents was left to the model-predicted diapycnal diffusivities (K_H), without a superimposed vertical advection. This is justifiable during the NEM by ECMWF winds that indicate minimal Ekman pumping (1.4×10^{-6} m/s) and by ascribing the observed low-frequency variation in sub-mixed-layer isotherm depth to subsurface horizontal advection associated with the residual mesoscale eddy field (Fischer, 1997). Similarly, phytoplankton sinking was not applied since a typical velocity of 1 m/d, characteristic of this period's smaller phytoplankton size-classes, would be at least an order of magnitude smaller than vertical redistribution due to the modeled diffusivities.

Physical Equations (Mellor and Yamada, 1982)

Momentum:

$$\frac{\partial U}{\partial t} - f_1(V - V_g) = \frac{\partial}{\partial z}\left[K_M \frac{\partial U}{\partial z}\right], \tag{1.1}$$

$$\frac{\partial V}{\partial t} + f_1(U - U_g) = \frac{\partial}{\partial z}\left[K_M \frac{\partial V}{\partial z}\right]. \tag{1.2}$$

Heat:

$$\frac{\partial T}{\partial t} - \frac{\partial}{\partial z}\left[K_H \frac{\partial T}{\partial z}\right] + \frac{1}{\rho c_p}\frac{\partial (I_0 + I_{IR})}{\partial z}. \tag{1.3}$$

Salt:

$$\frac{\partial S}{\partial t} = \frac{\partial}{\partial z}\left[K_H \frac{\partial S}{\partial z}\right]. \tag{1.4}$$

Phytoplankton and Nutrient Equations

Phytoplankton (N_a):

$$\frac{dN_a}{dt} = p_1 N_a - (z_1 + r_1)N_a + \frac{\partial}{\partial Z}\left[K_H \frac{\partial N_a}{\partial Z}\right]. \tag{1.5}$$

Nitrate (N_n):

$$\frac{dN_n}{dt} = -\frac{\rho_{N_n}}{\rho_N} p_1 N_a + \frac{\partial}{\partial Z}\left[K_H \frac{\partial N_n}{\partial Z}\right]. \tag{1.6}$$

Ammonium (N_r):

$$\frac{dN_r}{dt} = -\frac{\rho_{N_r}}{\rho_N} p_1 N_a + (\pi_1 z_1 + r_1)N_a + \frac{\partial}{\partial Z}\left[K_H \frac{\partial N_r}{\partial Z}\right]. \tag{1.7}$$

3.2. The penetrating component of Q_{SW}

The time-series of short-wave radiation (Q_{SW}) measured by a radiometer on the central mooring's surface buoy (Fig. 1) was used to calculate the penetrating component of heat flux (Eq. (1.3)). After allowing a 5% loss due to surface albedo, Q_{SW} was partitioned into the I_{IR} (45%) and I_0 (55%) components (Dickey and Simpson, 1983). Expressions for the vertical attenuation of these two components are shown in Eqs. (2.1) and (2.2).

Vertical attenuation of PAR:

$$I_0(z_{n+1}) = I_0(z_n)\mathrm{e}^{-(\kappa_w(z_n)+\kappa_c(z_n)\mathrm{Chl}(z_n))\mathrm{d}z}. \tag{2.1}$$

Vertical attenuation of infrared radiation:

$$I_{IR}(z) = I_{IR}(0)\mathrm{e}^{-z/\zeta}. \tag{2.2}$$

Total attenuation of I_0 consisted of a clear-water and a phytoplankton biomass (i.e., chlorophyll) component. A previously derived empirical expression for clear-water attenuation ($\kappa_W(z)$, Eq. (2.1)), based on the in situ irradiance profiles of Baker and Frouin (1987), was used (Wiggert, 1995). Chlorophyll specific attenuation ($\kappa_C(z)$, Eq. (2.1)) was based on the empirical relation of Morel (1988) and model-simulated Chl *a* profiles. Thus, vertical diffuse attenuation coefficients and the in situ light field are dynamic functions of the phytoplankton biomass predicted by the model, and provide a feedback pathway from biogeochemical components to physical components. Temporal variations in attenuation length for I_{IR} (ζ within equation) were based on determining solar zenith angle as a function of time of day, Julian day and latitude (Kirk, 1983). This resulted in 99% attenuation within the upper 1–4 m.

3.3. Growth rate limitation due to light

Phytoplankton growth rate (p_1, Eq. (3.1)) is taken as the product of the maximum phytoplankton growth rate (p_{max}) and the most limiting environmental variable, which is taken as either light or nutrients in this formulation.

$$p_1 = p_{max} \cdot \min[\rho_v, \rho_N] \tag{3.1}$$

Light limitation (ρ_v) is defined in Eq. (3.2):

$$\rho_v = \frac{I_0}{I_0 + p_{max}\Theta/a_{chl}\phi_m} \tag{3.2}$$

The second term in the denominator represents a half-saturation value, which is dependent on light intensity (I_0) via an expression for carbon to chlorophyll ratio (Θ, Eq. (3.3)):

$$\Theta = \left[\Theta_m^2\left(\frac{a_{chl}I_0\phi_m}{b_\Theta p_{max}}\right)^2\right]^{1/2} \tag{3.3}$$

This represents adjustments in phytoplankton physiology (i.e., changes in the number of photosynthetic units per cell) associated with changes in photon dosage (Kiefer, 1993). All of the remaining parameters appearing in Eqs. (3.2) and (3.3) are listed in Table 2.

3.4. Growth rate limitation due to nutrients

Total nutrient limitation (ρ_N in Eq. (3.1)) represents a combination of nitrate (ρ_{N_n}) and ammonium (ρ_{N_r}) limitation.

$$\rho_N = \rho_{N_n} + \rho_{N_r} = \frac{N_n e^{-\Psi N_r}}{\kappa_1 + N_n} + \frac{N_r}{\kappa_2 + N_r} \tag{4.1}$$

The exponential decay term in ρ_{N_n} is a commonly used form from the literature, which represents inhibition of nitrate uptake in the presence of elevated ammonium concentration (Wroblewski, 1977). Combining a definition of the *f*-ratio ($f = \rho_{N_n}/\rho_N$) (Fasham et al., 1990) with Eq. (4.1) results in the following expression for the inhibition parameter (Ψ):

$$\Psi = -\frac{1}{N_r}\ln\left[\left(\frac{f}{1-f}\right)\left(\frac{N_r}{K_2 + N_r}\right)\left(\frac{N_n + K_1}{N_n}\right)\right].$$

Measurements of mixed layer nutrient concentration and *f*-ratio acquired during TN043 at the hydrographic station nearest the moored array (S7) were used to determine the value of Ψ. For the observed range of N_r, Ψ ranges from 10.2 to 9.3, so a value of 9.75 was chosen (Table 2).

3.5. Application of the model

During the first part of the NEM, physical and bio-optical properties at the central mooring reflect the presence of significant mesoscale activity. Initial profiles from this time lead to misleading results in the 1-D model since the pycnocline is displaced upward 20–25 m, which is not typical of the observed conditions in the absence of superimposed mesoscale phenomena. Thus, this study of mixed layer and nutrient dynamics during the NEM has been constrained to 10 January through 4 February 1995 (Julian Day 10–35). The latter date coincides with the observed onset of thermal stratification within the surface waters (Fig. 2). The modeling run was terminated there since our primary interest was to study the dynamics of primary productivity and nutrient utilization during the NEM. The meteorological time-series from the central mooring's surface buoy were used as model boundary conditions of momentum, heat and buoyancy flux. Initial profiles of physical variables were based on in situ temperature, salinity and current-meter time-series from the central mooring (Fig. 1). Initial profiles of Chl*a* (not shown) and nutrient concentration (Fig. 8) were based on water samples obtained during TN043 at the station nearest to the moored array (station S7, see Fig. 1 in Morrison et al., 1998). Nitrate concentration within the

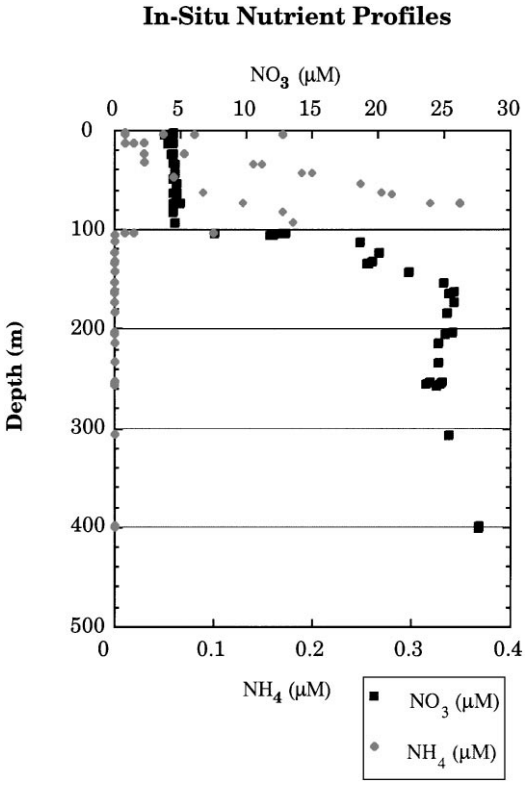

Fig. 8. Nutrient profiles used to develop the interdisciplinary model's initial condition. These data consist of all measurements taken during TN043 at the station nearest to the mooring (station S7). The high nitrate concentrations ($\geqslant 25$ μM) and lack of ammonium below the surface layer are evident.

mixed layer was 4–5 μM, while below 120 m it was 20–25 μM. Mixed layer ammonium was quite variable (0.01–0.35 μM) and non-existent at depth. Thus, the model's two initial nutrient profiles consist of uniform values both within and below the mixed layer and utilize an interpolation and smoothing scheme between the two regions.

The 1-D model was set up to run to a depth of 200 m, with 71 vertical levels. At depth, the vertical resolution is 3.4 m while within the upper 8.5 m there are 14 logrithmically spaced levels which allow for a more precise attenuation of the penetrating component of Q_{SW}. A salinity boundary condition was incorporated using Q_{LA} (latent heat flux) to estimate salinization of the surface waters resulting from surface evaporation driven by the NEM's low relative humidity. Such a boundary condition is often not employed in modeling applications since evaporation is typically not an important forcing mechanism. However, in the present case, it is a vital component of the vertical mixing which occurs during the NEM. Model runs that

either include (Case I) or exclude (Case II) the surface evaporation condition were used to assess its impact on the physical and biological components of the system. Finally, Case I boundary conditions were applied in model runs for which seasonal thermocline depth was increased. These simulations illustrate how the distribution of the biogeochemical constituents adjusts to changes in its vertical position, which could be caused by interannual variation in monsoon strength or subsurface mesoscale activity.

4. Results

4.1. *Case I*: *Application of the standard boundary conditions and assessment of model performance*

Fig. 9 shows the temperature and salinity time-series for the 25-day model period, chosen because of the minimal presence of mesoscale signatures that are at times quite prominent over the full observational period (Fig. 2). The moored measurements from the model period are consistent with the SeaSoar-based observations (Figs. 3b and 4b) in that they reveal a relatively homogeneous upper layer that extends to 90–100 m with strong vertical gradients in both properties just below this surface layer. The time-series also exhibit both the salinity inversion that develops between the surface layer and the deeper waters over the NEM (Figs. 4 and 9b) and temperature oscillations in the upper 10–15 m caused by diurnal heating (Fig. 9a). The moored time-series are used to provide initial profiles for the model's physical parameters, so the basically homogeneous upper layer is nicely reproduced in the simulations (Fig. 10).

Model-predicted temperature and turbulent diffusivity for Case I are shown in Fig. 10a. The model reproduces two vertical mixing events, labeled M1 and M2, that appear in the observations over JD 16–18 and JD 19–21 (Figs. 9 and 10). In the temperature time-series, these features appear most prominently as changes in depth of the 25.08°C isotherm, with M2 also having a distinct salinity signature (Fig. 9). Case I temperature results reproduce M1 with the shoaling of the 25.1°C and 25.03°C isotherms, while M2 coincides with the shoaling of the 25.02°C isotherm. Additionally, the modeled diffusivities show the largest magnitudes and deepest penetration depths in conjunction with M1 and M2 (Fig. 10a). Over JD 24–25, a third mixing event (M3) is apparent in the time-series (Fig. 9). A strikingly similar feature appears in the model results as a deepening of the 25.03°C isotherm, although it occurs one day earlier than observed in situ (Fig. 10a).

The model results show near-surface temperature gradients that are stronger than indicated by the in situ measurements. In addition, temperature between 25 and 90 m is slightly lower in the simulations, although it is essentially homogeneous in both the model and the observations (Figs. 9 and 10). These characteristics indicate that the model is trapping too much heat within the upper 5–10 m and that convective mixing in the model may be too penetrative. Over the last week of the modeled period, the near-surface heat trapping contributes to the onset of seasonal stratification (Fig. 10)

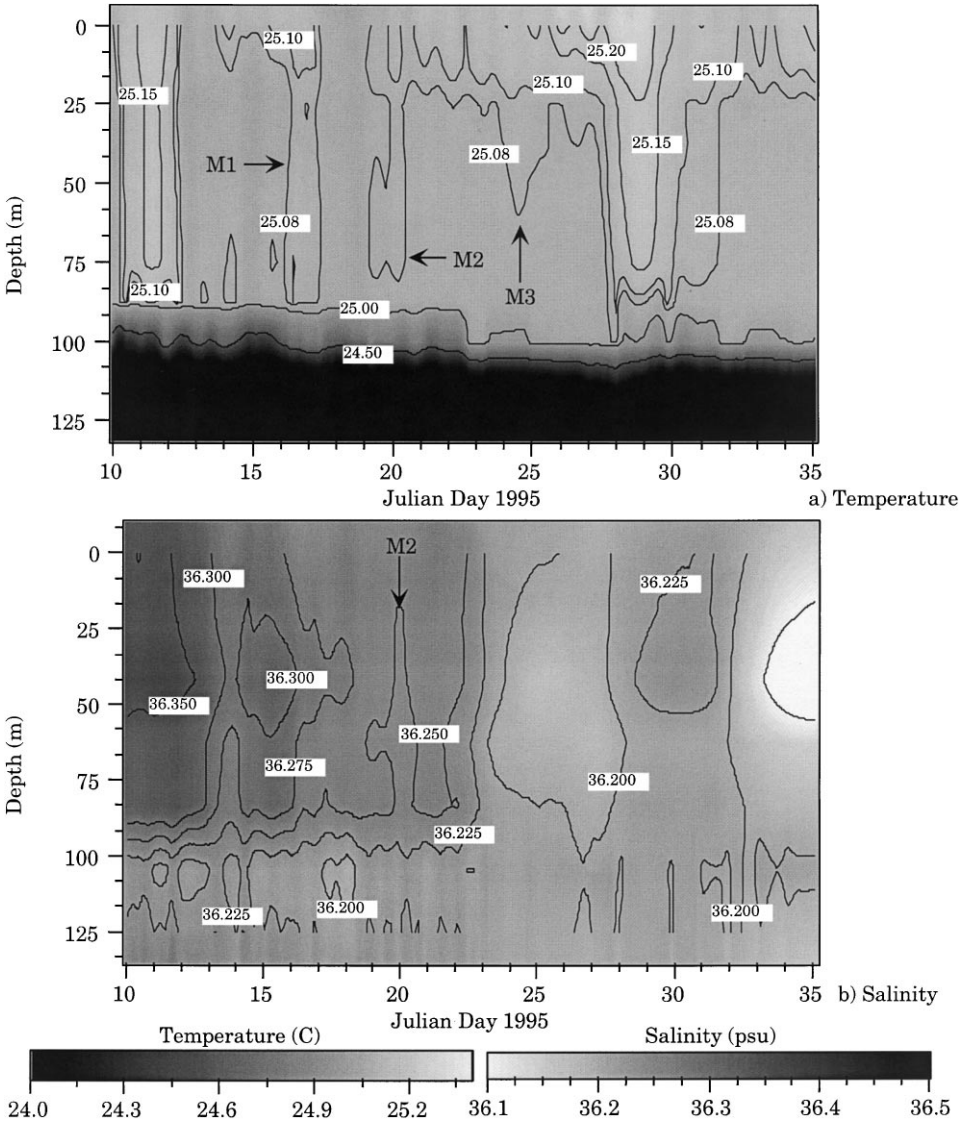

Fig. 9. High resolution (a) temperature (°C) and (b) salinity (psu) from moored time-series during winter convection. The data presented here are from the period chosen for the model runs. The advective signature within these data has been removed by applying a running mean to the 100 m time-series and subtracting this from all data. The magnitude was recovered by adding the 25 day mean from 100 m. In order to highlight the water column's inherent propensity toward salt-fingering, the gray scales were chosen such that darker regions represent T–S characteristics which individually lead to increased density.

that directly contrasts the ongoing deep convection observed in the moored time-series (Figs. 5 and 9). Diurnal heating of the sea surface is also evident in both the observations and the model results, though it is more pronounced in the latter. This

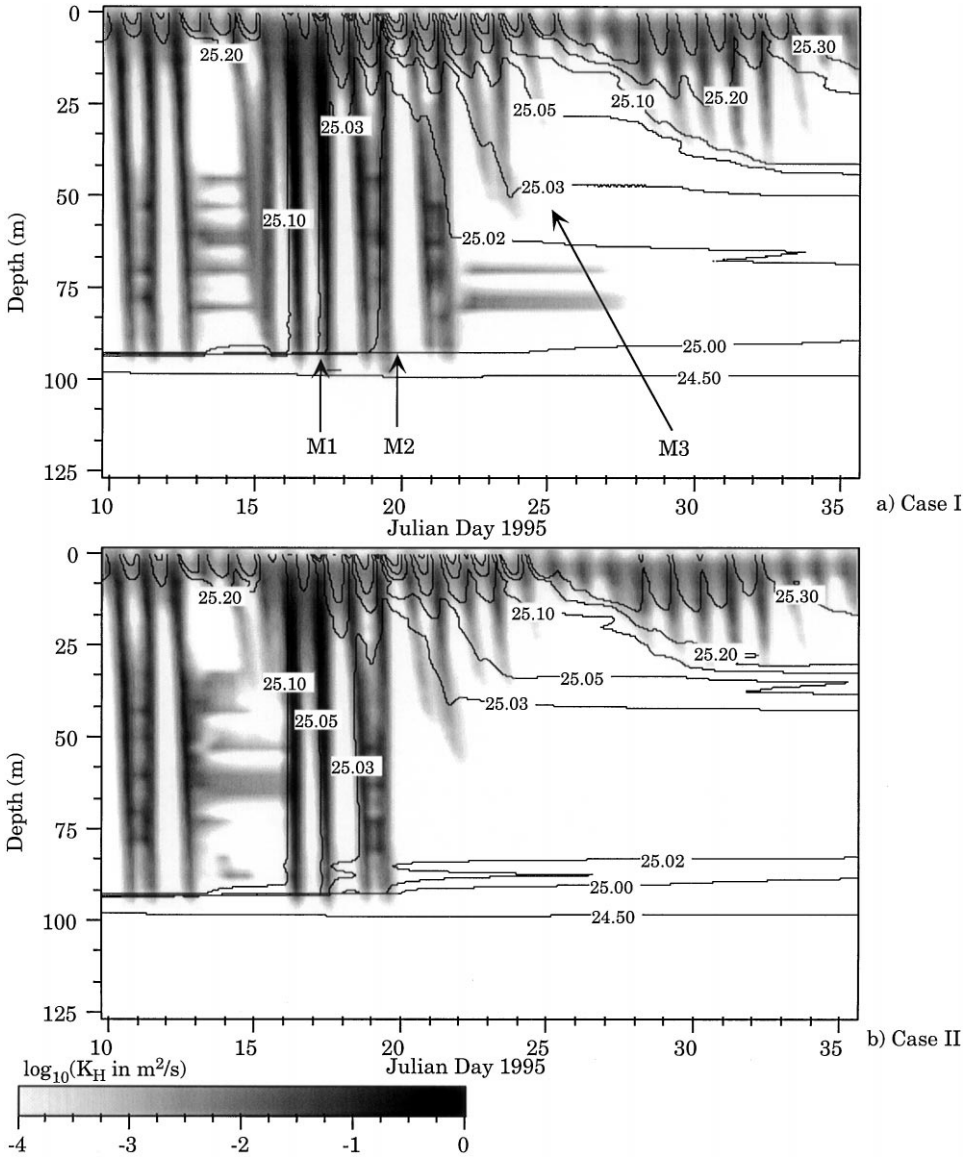

Fig. 10. Temperature and turbulent diffusivity (K_H) as predicted by the (a) Case I and (b) Case II model runs. Values of K_H have been log transformed. The isotherms and the diffusivities clearly reveal the diurnal cycle of the daytime formation of surface stratification followed by deep nighttime mixing. The diffusivities emphasize the sensitivity of the thermal structure to the mixing enhancement provided by including the evaporation boundary condition (Case I). This is best represented by comparing the penetration depth of elevated K_H during the three noted mixing events (M1–M3).

leads directly to the large-magnitude, daily oscillations in Z_{ML}, as the daytime surface heat flux counteracts the destabilizing tendency of the evaporation-induced surface salinization.

Mooring-based Z_{ML} time-series reveal diurnal cycling from 10–15 m down to 90–100 m for most of the modeled period (Fig. 5a). Model-predicted Z_{ML}, based on a ΔT of both 0.1°C and 0.3°C, provides an additional means of assessing the model physics (Fig. 5b). The 0.1°C criterion reflects the shoaling of the mixed layer, which occurs toward the end of the model run, while the 0.3°C criterion more prominently reflects the deep diurnal cycling seen in the time-series. The latter criterion also illustrates the model's ability to capture, over the first 10 days of the run, two periods for which the mixed layer did not shoal during the day. The specific timing of these two periods does not precisely correspond between the model and the observations, yet their duration and the duration of the intervening period is decently reproduced. Finally, the model reasonably captures the vertical extent of the mixed layer's diurnal variation. The most conspicuous discrepancy may be seen in the minimum depth of the 0.1°C Z_{ML}, which is generally below 10 m in the observations but which is consistently near 5 m within the model results. This discrepancy between the minimum observed and modeled Z_{ML} is again related to the model's tendency toward near-surface trapping of heat.

The chlorophyll *a* (i.e., phytoplankton) distribution reflects the stratification and vertical mixing that occur during the simulation (Fig. 11a). A doubling in near surface chlorophyll *a* coincides with an intensification in diurnal surface heating prior to JD 15 (Figs. 10a and 11a). Additionally, the M1 and M2 events act to uniformly redistribute chlorophyll *a* over the upper 80 m (Fig. 11a). Following these two mixing events, stratification intensifies and chlorophyll *a* continually increases within the mixed layer through JD 22 (disregarding the expected near-surface diurnal oscillations). Mixed-layer accumulation of phytoplankton biomass is best illustrated by the descent of the 0.35 mg Chl a/m^3 isopleth down to the base of the mixed layer (90 m). However, upon reaching this depth it quickly shoals to 55 m and continues to rise with time. The isopleth's shoaling is indicative of an ongoing accumulation of near-surface chlorophyll *a* that significantly reduces subsurface PAR via increased attenuation. The permanent shoaling of the modeled mixed layer immediately follows and a typical spring phytoplankton bloom proceeds to develop (Figs. 5b, 10a and 11a).

Prior to the spring bloom, a striking characteristic of the modeled primary productivity is that both ammonium and *f*-ratio indicate that phytoplankton growth was essentially driven by ammonium uptake (Fig. 12). Variability in near surface ammonium concentration is consistent with the variability exhibited in chlorophyll *a* (Figs. 11a and 12a). The stratification that develops prior to JD 15 results, via stimulation of phytoplankton growth, in a reduction from 0.2 to 0.1 μM in near-surface ammonium with reduced values extending below 25 m (Fig. 12a). Associated with this surface increase in biomass is an accumulation of ammonium below 50 m, due to reduced irradiance at depth that allows the loss terms (i.e., $\pi_1 z_1$ and r_1, Eq. (1.7)) to dominate. The *f*-ratio within the mixed layer is $\leqslant 0.2$ except within the near-surface region of ammonium depletion (Fig. 12b). A reduction in nitrate-uptake

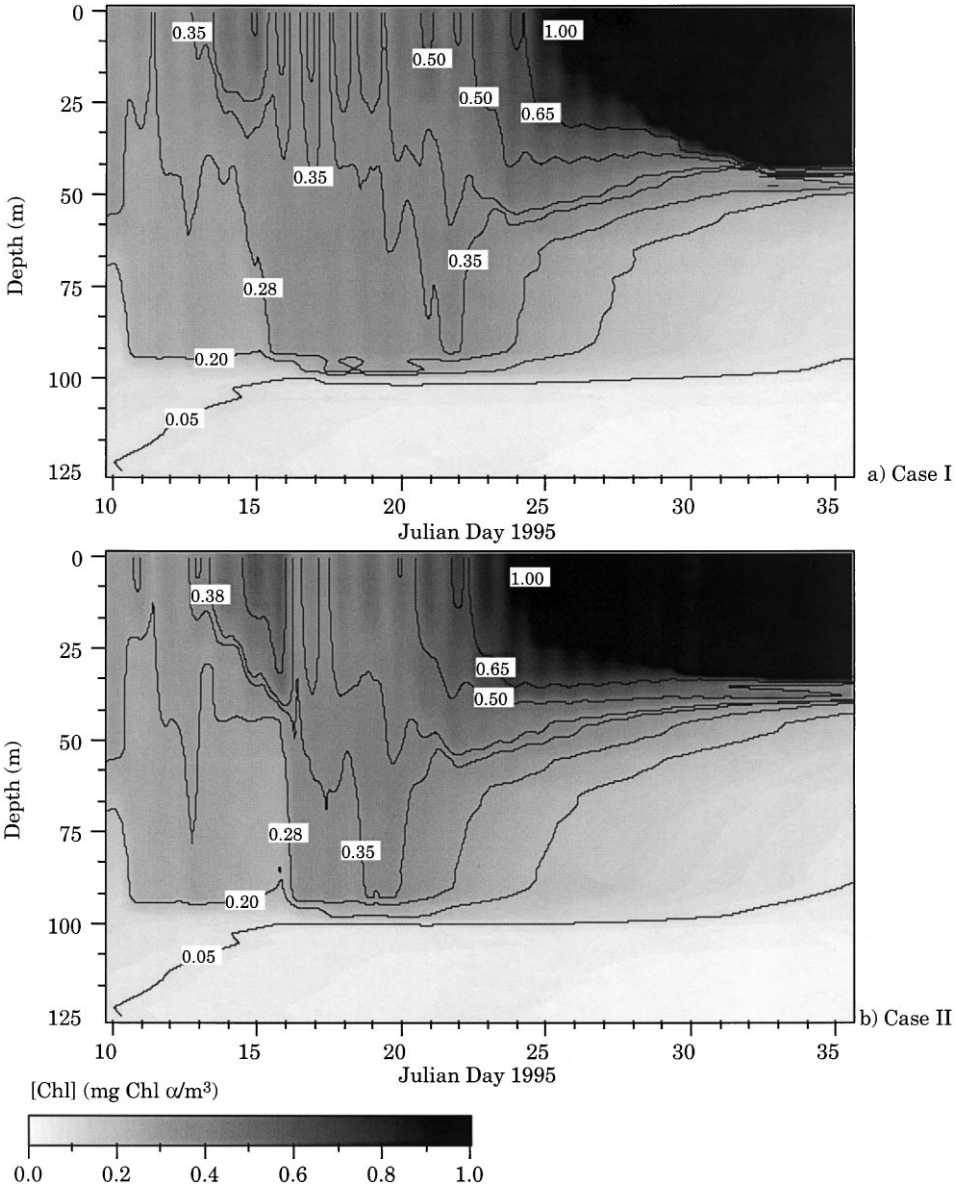

Fig. 11. Chlorophyll *a* as predicted by (a) Case I and (b) Case II model runs. These indicate a diurnal cycle in surface chlorophyll *a* resulting from a combination of diel photosynthetic processes and the diurnal mixing processes. The additional stratification in Case II results in a notable increase in areal chlorophyll *a*. This is best illustrated by intercomparing the descent of the 0.35 mg Chl a/m^3 isopleth.

inhibition is associated with the reduced concentration of surface ammonium and leads to a slight increase in *f*-ratio, although values remain below 0.3. The two days of deep convection that follow this event (JD 16–18, Fig. 10a) result in a re-homogenization of

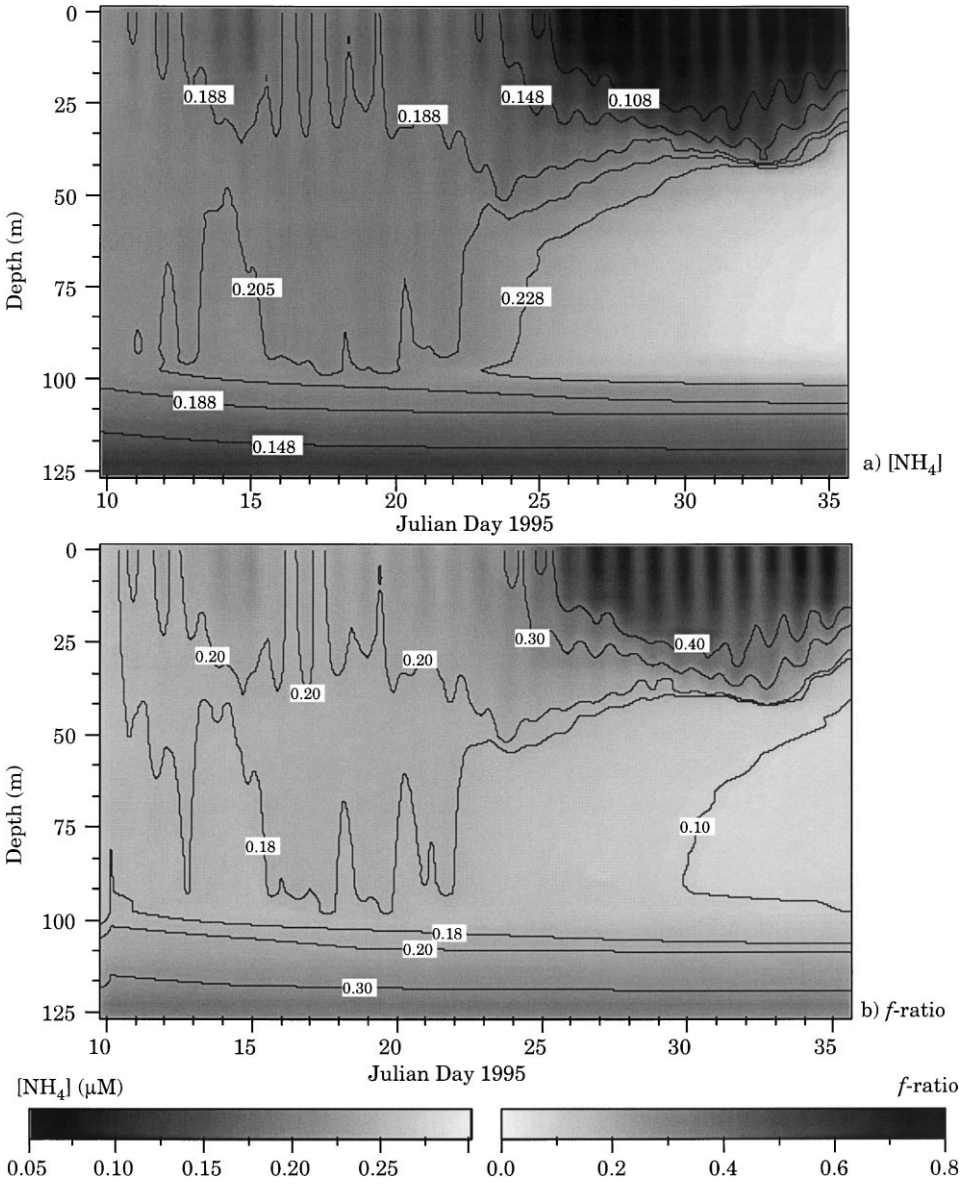

Fig. 12. (a) Ammonium concentration and (b) *f*-ratio for the Case I model run. These reflect the relatively consistent cycle of ammonium uptake and regeneration which coincides with the diurnal cycle of stratification during the day and deep convective mixing at night. With the permanent establishment of stratification (JD 25), a transition in nutrient characteristics is triggered whereby ammonium in the surface waters decreases with a corresponding increase in *f*-ratio. These indicate that a transition to increased nitrate uptake (new production) is underway.

ammonium over the upper 90 m (Fig. 12a) to a concentration consistent with the initial condition (Fig. 8). A diurnal cycle, consisting of ammonium uptake and increasing *f*-ratio within surface waters during the photoperiod followed by a vertical re-homogenization due to nighttime mixing, appears over JD 16–20. It is interesting to note that this period coincides with the significant reduction in diurnal stratification indicated within the time-series of Z_{ML} (Fig. 5). As stratification intensifies and the mixed layer permanently shoals in the model (Figs. 5b and 10a), ammonium within the upper layer is utilized and *f*-ratio continuously rises (Fig. 12) as nitrate utilization within the model increases.

4.2. *Case II*: *The impact of surface evaporation on vertical mixing and its redistribution of biogeochemical properties*

Case II boundary conditions are identical to those applied in Case I, except for the removal of evaporation based on Q_{LA}. Intercomparison results from the two boundary condition cases reveals how evaporation leads to enhanced vertical mixing that impacts the physical structure of the water column and the distribution of the biogeochemical constituents. Within the temperature distribution, enhanced mixing leads to cooler temperatures over the upper 90 m when evaporation is included (Fig. 10). Cooler temperatures are illustrated by both the 25.05°C isotherm, which penetrates beyond 25 m about a week later in Case I, and the 25.2°C isotherm, which remains above 25 m in Case I but deepens beyond 25 m after JD 29 in Case II. Another prominent difference between the two temperature fields is the evolution of the 25.02°C isotherm which shoals to about 15 m and remains above 60 m after the M2 mixing event (JD 19) but never gets higher than 80 m throughout Case II simulation. Fig. 13 shows positive values of the temperature difference between Cases I and II simulations, thus highlighting where and when evaporation leads to warmer temperatures. This figure's two most striking features are the lack of positive ΔT's above 90 m and the steady increase in ΔT below 90 m. The two positive ΔT features over JD 10–17 in the upper 90 m reflect enhanced downward mixing of heat in Case I that is trapped at the surface in Case II.

The difference in temperature between Cases I and II can be attributed to a very slight variation in the penetration depth of elevated turbulent mixing within the simulations (Fig. 10). A precise comparison between the two cases of the diffusivity distribution associated with the M2 event shows that in Case I, the elevated mixing penetrates to the depth of the 24.5°C isotherm, while in Case II this depth is not achieved. The difference in penetration depth between the two cases is 3 m or less. However, due to the strong thermal stratification at that level, a significant difference in the mean temperature of the entrained water is realized (Figs. 10 and 13). A similar small variation in penetration depth is associated with the M1 event, with a comparable result regarding the evolution of the 25.03°C isotherm. The most noticeable difference between the two cases is the vertical extent of elevated diffusivities over JD 20–21 and JD 22–23. These more prominently illustrate the sensitivity to application of the salinity boundary condition but do not have as great an impact as the slight variation in penetration depth noted for events M1 and M2.

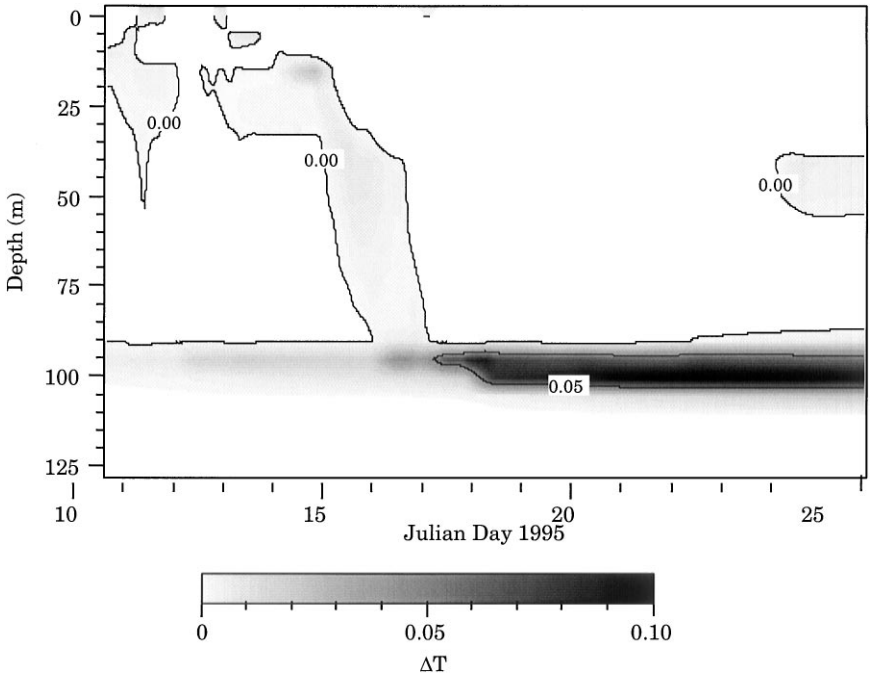

Fig. 13. Difference in temperature between the model runs with and without the inclusion of the evaporation boundary condition. Only positive differences are represented. These reveal when Case II boundary conditions (i.e., exclusion of evaporation) led to warmer temperatures because of the reduced vertical mixing. This is especially prevalent at the base of the pycnocline where the increased penetration provided by the evaporation condition led to greater entrainment of cooler waters from below the surface layer.

The reduced turbulent mixing that occurs when the evaporation condition is not applied leads to distinct differences in the modeled chlorophyll *a* distribution (Fig. 11). Due to enhanced vertical mixing, Case I chlorophyll *a* concentrations below 25 m generally increase faster through the first week of the model run (note the 0.28 mg Chl a/m^3 isopleth) while Case II chlorophyll *a* concentrations above 25 m are higher. Following JD 17, the 0.35 and 0.38 mg Chl a/m^3 isopleths indicate a significant divergence in areal phytoplankton biomass over the course of the two model runs (Fig. 11). This is better quantified by Case II to Case I ratio of areal chlorophyll *a* concentration, which shows a consistent 5% increase for Case II over JD 16–21 (Fig. 14). The differences in vertical mixing intensity also impact the timing and vertical characteristics of the phytoplankton bloom that occurs over approximately the last 10 days of the two model runs. Case II bloom occurs 1–2 days sooner with the 0.65 and 1.0 mg Chl a/m^3 isopleths initially penetrating 5–10 m deeper (Fig. 11). The initial appearance of the 0.65 mg Chl a/m^3 isopleth for Case II (Fig. 11b) coincides with the development of areal chlorophyll *a* concentrations that are more than 5% greater than those for Case I (Fig. 14). The difference between the areal values for these

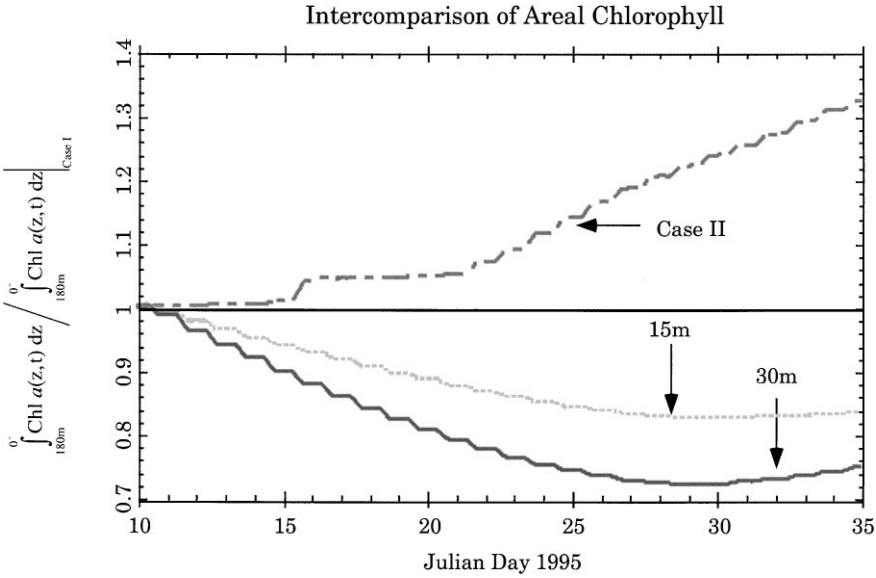

Fig. 14. Normalized time-series of areal chlorophyll *a*. Normalization consists of determining the ratio for a given modeling run (Case II, 15 m or 30 m) to the standard run (Case I). These time series illustrate how the variation in boundary and initial conditions applied in these numerical studies affected the accumulation of phytoplankton biomass in the water column.

two numerical experiments increases continuously from this point through the end of the simulations.

4.3. Impact of the thermocline's downward displacement

Numerical simulations using the standard (i.e., Case I) boundary conditions and downward thermocline displacements of 15 and 30 m were performed in order to investigate a possible means of generating the observed interannual variation in phytoplankton biomass and primary productivity. The thermocline's position is taken to be at the base of the surface layer indicated in the SeaSoar observations of temperature, salinity and chlorophyll *a* from TN044 (Figs. 3b, 4b and 7b) and the nutrient profiles from TN043 (Fig. 8). Except for chlorophyll *a*, all initial profiles for these simulations (i.e., temperature, salinity, currents, nitrate and ammonium) were adjusted to reflect the downward shifts in thermocline depth. Since it is not solely determined by bulk water-column stratification, the chlorophyll *a* profile was not altered in order to keep intercomparison of the modeled chlorophyll *a* distributions relatively straightforward.

The resulting chlorophyll *a* distributions for these thermocline displacement studies (Fig. 15) illustrate that significant alterations in the vertical distribution of chlorophyll *a* are effected as the position of the upper limit of the thermocline is changed. Since these simulations employ Case I boundary conditions (i.e., surface evaporation is included),

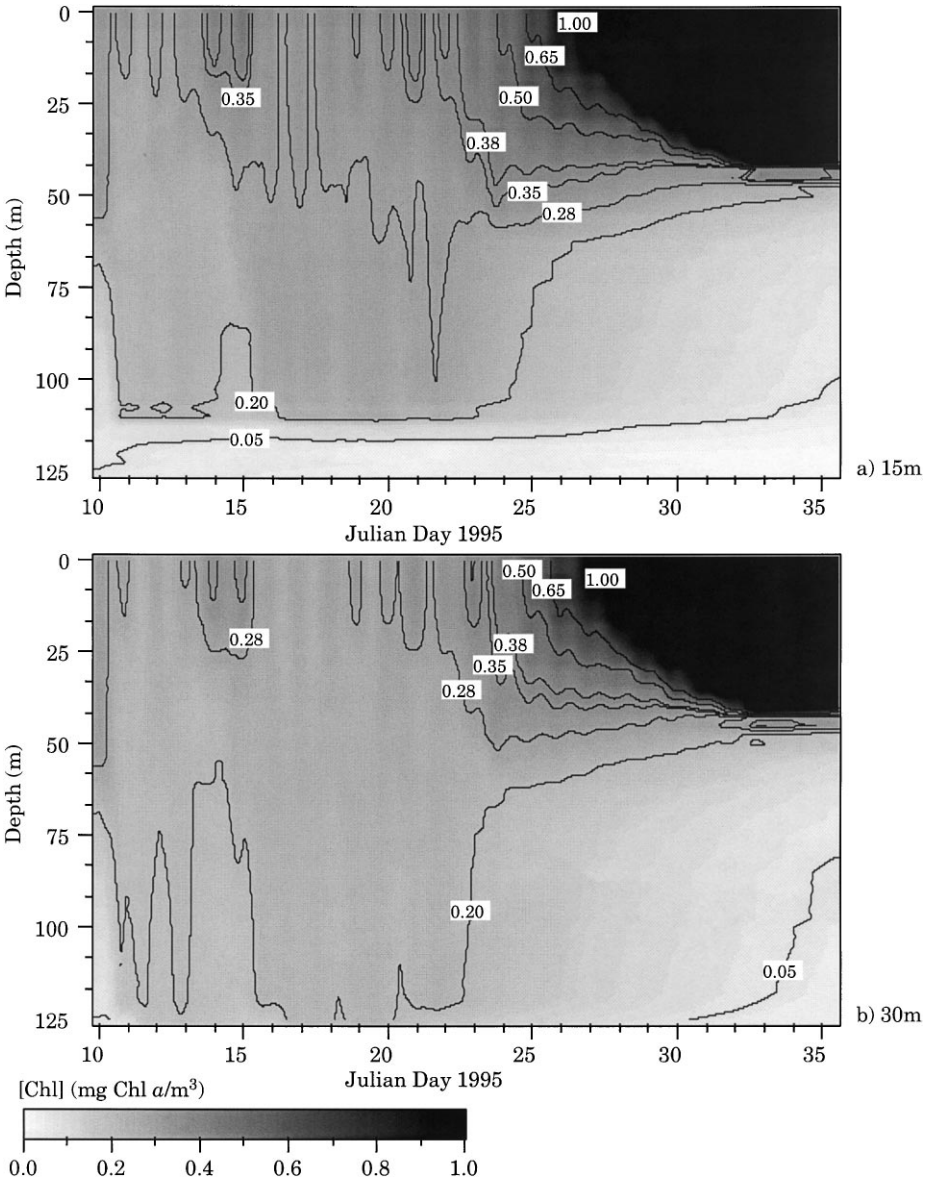

Fig. 15. Chlorophyll *a* for two model runs where pycnocline depth was increased by (a) 15 and (b) 30 m. These indicate that a significant reduction in surface chlorophyll *a* occurs as daily PAR dosage is reduced by the deeper pycnoclines. This underscores the impact of the near surface pycnocline on phytoplankton growth and provides a possible mechanism for generating the interannual variability in primary productivity and chlorophyll *a* that has been observed in this region.

Case I chlorophyll *a* distribution is considered the intercomparison standard (Fig. 11a). Differences between Case I and the two downward-displacement simulations are best illustrated by the evolution of the 0.28 mg Chl a/m^3 isopleth. For Case I (Fig. 11a), surface values only briefly drop to this level (JD 11) while over JD 15–20, concentrations are at least 0.28 mg Chl a/m^3 through 80 m. For a 15 m thermocline displacement (Fig. 15a), the 0.28 mg Chl a/m^3 isopleth reaches the surface diurnally prior to JD 15 and during the M1 mixing event (JD 16 and 17, Fig. 10a). Otherwise, after JD 15 it ranges from 40–70 m with one brief excursion down to 100 m (JD 22). For a 30 m thermocline displacement (Fig. 15b), the 0.28 mg Chl a/m^3 isopleth is not permanently established prior to JD 22.

Thermocline depth has relatively little impact on this bloom's timing. The development of chlorophyll *a* concentration $\geqslant 1$ mg Chl a/m^3 shows a 2-day difference between Case I and the 30 m displacement result. This time lag is due to the lower near-surface chlorophyll *a* concentrations in the latter modeling experiment when permanent stratification initiates. It is interesting to note the difference in the rates at which the spring phytoplankton bloom develops within the three model runs. In the 30 m displacement result (Fig. 15b), a three-fold increase in chlorophyll *a* concentration leading to the bloom occurs over a 4-day period (i.e., the time elapsed between the surface appearance of the 0.35 and the 1.0 mg Chl a/m^3 isopleth). This takes 8 and 5 days for Case I and 15 m thermocline displacement results, respectively (Figs. 11a and 15a). Thus, the elapsed time for this three-fold increase to occur varies inversely with displacement depth. However, this reflects when surface concentrations $\geqslant 0.35$ mg Chl a/m^3 develop in each model run and indicates a significant reduction in areal biomass accumulation as the upper thermocline is displaced downward. Fig. 14 also shows the intercomparison between time series of areal biomass for the two thermocline displacement simulations and the standard run (Case I). These experiments indicate a 15–30% reduction in areal biomass, in comparison to Case I. Since these simulations do not extend over the entire NEM, the noted reductions could easily translate to the 5–6 fold range present in CZCS imagery from the late NEM. The reduction in areal biomass is attributed to decreased daily PAR associated with the increased extent of vertical mixing, since upper layer nutrient concentrations were non-limiting despite being somewhat reduced by the thermocline displacements.

5. Discussion

Surface forcing during the Northeast Monsoon generally consists of moderate wind-driven mixing, a net flux of heat from the ocean to the atmosphere, and elevated evaporation. This forcing drives deep convective mixing that reaches, and proceeds to erode, the permanent thermocline in the northern Arabian Sea. This mixing acts to transport nitrate into the surface waters. Throughout the world's oceans, nutrients transported via this wintertime mixing fuel the subsequent spring phytoplankton bloom when seasonal stratification is reestablished. However, there is mounting evidence that, within the Arabian Sea, convective mixing and significant primary

production can occur simultaneously. The SeaSoar observations presented here show a deepening of the surface layer from 50 to 110 m coincident with an accumulation in phytoplankton biomass over the course of the NEM. Hydrographic data from the intervening process cruise show surface nitrate concentrations $> 4\,\mu M$ extending 1000 km offshore while the mean value of primary production determined during this cruise was $1.64\,gC/m^2/d$ (Barber et al., 2000). In another recent study, wintertime primary productivity of up to $807\,mgC/m^2/d$ was measured in the northeastern Arabian Sea and attributed directly to the entrained nutrients (Madhupratap et al., 1996).

However, the nutrient uptake experiments performed during TN043 (McCarthy et al., 1999) indicate that photosynthesis during the NEM depends primarily on regenerated nitrogen despite the elevated nitrate concentrations within the mixed layer. This is due to ammonium concentrations that are sufficient to inhibit nitrate uptake. Predominantly regenerated production despite replete concentrations of nitrate is an interesting nutrient utilization mechanism that all of our modeling experiments support. Prior to the model-predicted spring bloom, nitrate uptake rates attain maximal instantaneous values of $0.15\,\mu M/d$ during the photoperiod. The model's ammonium and *f*-ratio distributions are consistent with the in situ observations and indicate a diurnal cycle consisting of ammonium uptake during photosynthesis and ammonium regeneration via grazing and other losses. A key component of the coupling between the physical and biological processes appears to be the extensive diurnal cycling of the mixed layer (10–100 m) observed in the moored time-series and captured by the interdisciplinary model. The importance of this diurnal behavior also is supported by recent 3-D modeling studies of the Arabian Sea by McCreary et al. (2000) in which the incorporation of a diurnally varying mixed layer improved the post-NEM phytoplankton bloom. Our numerical simulations suggest that during the NEM, full utilization of the available nutrients is prevented by diurnal (nighttime) penetration of the mixed layer below the euphotic zone (the 1% light depth is 65–70 m). This cycling in Z_{ML} dilutes the near surface phytoplankton concentration and allows for the production of ammonium in the lower half of the surface layer. Thus, it appears that while phytoplankton growth is promoted during daytime stratification, a accumulation of phytoplankton biomass is restrained by the mixed layer's diurnal cycling despite euphotic zone nitrate concentrations that remain elevated. This diurnal dilution of phytoplankton biomass further suggests a mechanism for transporting particulate matter downward and out of the surface layer. However, this does not appear to be a significant contributor to the observed export fluxes at depth (Gardner et al., 1999).

The combination of low nitrate uptake rates and deep convective mixing suggests that the mixed layer may be undergoing net nitrate enrichment while supporting the elevated primary production. The four model results presented here indicate that areal nitrate utilization prior to the bloom is relatively balanced with vertical entrainment. In fact, the nitrate distribution is quite sensitive to which model configuration is employed. Cases I and II result in a slow uptake of nitrate whereas the two thermocline displacement cases indicate enrichment of the mixed layer. Additional runs not presented here indicate that this balance is also sensitive to the constant value chosen

for background turbulent diffusivity. A slight (e.g., one-half order of magnitude) increase in background diffusivity (K_H and K_M, Eqs. (1.1)–(1.7)) leads to noticeably enhanced enrichment. Underprediction of interior (i.e., sub-mixed-layer) turbulent diffusivities has previously been noted as a model limitation in terms of its ability to accurately transport heat from the surface boundary layer into the upper thermocline (Kantha and Clayson, 1994; Large et al., 1994). Another limitation of the physical model is that no provision for double diffusion mechanisms has been included. The SeaSoar salinity measurements clearly show that NEM evaporation results in significant salinization of the surface layer and a salinity profile that is prone to salt fingering. If double diffusion mechanisms were incorporated, vertical mixing could take place more consistently throughout the day and would be less dependent upon the onset of nighttime cooling. This could lead to a less frequent occurrence of diurnal mixed layer shoaling, which would serve to reduce phytoplankton growth rates. Interestingly, the model does predict more frequent shoalings than indicated in the observed Z_{ML} time-series (Fig. 5).

An overriding theme of these modeling experiments has been the sensitivity of the development of stratification to the choice of model configuration. Exclusion of the evaporation boundary condition resulted in appreciable increases in the degree of water column stratification and reduced the penetration depth of the convective mixing by about 3 m. These numerical experiments indicate that this slight change in penetration depth significantly impacts total entrainment of cooler, high-nitrate waters from below the mixed layer. Omission of the evaporation condition also led to an increase in near surface phytoplankton biomass since the reduced mixing raised the daily dose of PAR, even though nitrate flux into the euphotic zone was reduced. In addition, initiation of the spring phytoplankton bloom, as defined by the appearance of the 1 mg Chl a/m^3 isopleth, was accelerated in the absence of evaporation (Fig. 11) although the associated reduction in nitrate flux is likely to reduce the bloom's magnitude significantly. Thus, it appears that the elevated evaporation serves to increase total primary production during the NEM, in addition to significantly contributing to the region's physical setting through its role in the formation of Arabian Sea High Salinity Waters (Rochford, 1964; Shetye et al., 1994; Kumar and Prasad, 1999).

These model results suggest another consideration in the effort to better understand open ocean ecosystems. For years when chlorophyll *a* concentrations in this region are $< 1\ mg/m^3$ (Kabanova, 1968; Banse, 1987; Bauer et al., 1991), the Arabian Sea could be classified as a high nutrient – low chlorophyll (HNLC) region since upper layer nitrate concentrations are $> 4\ \mu M$ during the height of the NEM. Several explanations for HNLC regions have been put forward including iron limitation (Martin et al., 1991; Landry et al., 1997), grazing control of phytoplankton (Cullen et al., 1992), and silicon limitation (Dugdale et al., 1995). In our model, regulation of phytoplankton growth is due to the combined effect of the diurnal mixed layer oscillation and grazing pressure. We have assumed a uniform grazing rate throughout the water column, which may not be realistic. However, the model does maintain ammonium concentrations (and *f*-ratios) that are consistent with the observations and of sufficient magnitude to inhibit nitrate uptake. Once the water column begins to

stratify permanently, the growth rate of phytoplankton exceeds the applied rate of zooplankton grazing. Thus, phytoplankton biomass accumulates, the available ammonium is consumed, and utilization of the nitrate pool commences. Within the natural system it might be argued that silicon limitation could play a role, particularly since nitrate/silicate ratios are $\geqslant 2$ at the base of the mixed layer (Jones, unpublished data). But toward the surface, nitrate/silicate decreases rapidly to < 1, indicating that nitrate is more likely to be limiting. Finally, no provision for iron limitation has been made in the formulation of the interdisciplinary model since it is not considered to be a concern given the significant aeolian input of dust from the desert regions of Africa and the Arabian Peninsula during the SWM (Measures and Vink, 1999).

Given the previous in situ measurements, the magnitude of NEM primary productivity during the 1995 Arabian Sea Expedition was up to 5-fold higher than expected (Ryther et al., 1966; Kabanova, 1968; Banse, 1987; Barber et al., 2000). This range may result from significant interannual variability in phytoplankton biomass during the NEM (Banse and McClain, 1986). Near-surface proximity (within 100–150 m) of a sharp, permanent thermocline and nutricline could be a source of such interannual variability if its depth undergoes significant interannual modulation. This might be accomplished by variations in intensity of the monsoon cycle or the presence of persistent subsurface mesoscale features spawned by the energetic coastal upwelling of the SWM. Indeed, the latter scenario is indicated in the moored time-series. The cool subsurface mesoscale feature that appears in the temperature data during the first half of the NEM (JD 305–330, Fig. 2) coincides with the maximum near-surface chlorophyll-fluorescence values recorded by the moored fluorometers (see Fig. 7 in Dickey et al., 1998). Similarly, modeling experiments incorporating 15 and 30 m downward displacements of physical and nutrient mixed layer values reveal a 2–3 fold reduction in surface chlorophyll *a* prior to the model's spring phytoplankton bloom. These thermocline displacement experiments underscore the importance of the near-surface presence of the nutricline to the overall productivity of the central Arabian Sea (Ryther and Menzel, 1965) and present a possible means of generating the significant interannual variability which has been observed in this region during the NEM.

Finally, we note that near the mooring, nitrite (NO_2) concentrations in the upper 100 m were relatively homogeneous and appear to have accumulated over the course of the NEM. The mean upper-layer nitrite concentration during TN042 was 0.1 μM, whereas during TN043 and TN044 mean concentrations of 0.4–0.7 μM were observed. Additionally, the hydrographic section of nitrite from TN043 (similar to Fig. 6) shows concentrations above 0.3 μM over the upper 60 m that extend 900 km offshore and concentrations above 0.4 μM in the upper 50 m between 500 and 800 km offshore. These nitrite values from the latter stages of the NEM were 10–20% of the coincident nitrate concentrations and about twice as high as the coincident ammonium concentrations. The source of this nitrite and its function in the region's nitrogen cycle needs clarification. McCarthy et al. (1999) report elevated nitrification rates in the lower half of the surface layer that point to ammonium oxidation as a means of in situ production. Nitrite also could be entrained from the secondary nitrite maximum associated with the suboxic regions that are characteristic of the northeastern Arabian Sea (Naqvi et al., 1992). This could indeed be occurring since, during TN043, nitrite

concentrations $\geqslant 1.0\ \mu M$ were observed as shallow as 170 m within 200 km of the mooring. A third nitrite source could be the arrested assimilation of nitrate during photosynthesis (Olson et al., 1980). Since *f*-ratios measured during TN043 were $\leqslant 0.2$, this is an unlikely mechanism in the latter stages of the NEM. However, it would appear that *f*-ratios decreased over the NEM (maximum ammonium concentrations during TN042 were an order of magnitude lower than in Fig. 6b), so nitrite production via arrested nitrate assimilation would be more feasible during the early stages of the NEM. No matter the source, nitrite-uptake rates should be rather low since, even at equivalent concentrations, nitrate uptake has been reported to be 5 times higher (Kiefer and Kremer, 1981). Thus, any source of nitrite to the upper layer during the NEM will result in an accumulation. Given the low rates of nitrite uptake relative to those of ammonium and nitrate, we feel justified in not including nitrite pathways within the interdisciplinary model for the chosen time domain. Over more extensive time periods, studies of nitrogen cycling in this region would require a careful accounting of nitrite source(s) since nitrite derived from nitrification should be considered 'recycled' nitrogen whereas entrained nitrite or nitrite arising from arrested nitrate assimilation should be considered 'new' nitrogen.

Acknowledgements

This research was supported by ONR grants N00014-94-1-0362 (BHJ), N00014-96-1-0505 (TDD), N00014-94-1-0226 (KHB), N00014-94-1-0161 (RAW), N00014-94-1-0450 (JM) and NSF grants OCE9310577 and OCE9712577 (LAC). JDW was supported during the preparation of this manuscript by USRA contracts NAS5-32484 and NAS5-98181. Miguel Maccio and Marcela Stern (LDEO), Derek Manov and Dave Sigurdson (UCSB) and Frank Bahr, Will Ostrom and Rick Trask (WHOI) provided technical assistance was during the fieldwork. Assistance with the data utilized here was provided by Zackary Johnson (Duke University), Cheng Ho and Chris Kinkade (LDEO), Jan Gundersen (TAMU), Dave Sigurdson and Sarah Zedler (UCSB), Zhihong Zheng (USC) and Frank Bahr and Mark Baumgartner (WHOI). The manuscript has benefited from discussions with Kevin Arrigo, Jim Christian, Dale Kiefer, Craig Lee and Chuck McClain. We would also like to express our gratitude to Sharon Smith for her much appreciated support. Finally, the comments and suggestions of the reviewers were quite helpful and greatly appreciated. This is US JEGOFS Contribution Number 486.

References

Baker, K.S., Frouin, R., 1987. Relation between photosynthetically available radiation and total insolation at the ocean surface under clear skies. Limnology and Oceanography 32, 1370–1377.

Banse, K., 1987. Seasonality of phytoplankton chlorophyll in the central and northern Arabian Sea. Deep-Sea Research 34, 713–723.

Banse, K., McClain, C.R., 1986. Winter blooms of phytoplankton in the Arabian Sea as observed by the Coastal Zone Color Scanner. Marine Ecological Progress Series 34, 201–211.

Barber, R.T., Marra, J., Bidigare, R.R., Codispoti, L.A., Halpern, D., Johnson, Z., Smith, S.L., 2000. Primary productivity and its regulation in the Arabian Sea during 1995. Deep-Sea Research II (in press).

Bauer, S., Hitchcock, G.L., Olson, D.B., 1991. Influence of monsoonally-forced Ekman dynamics upon surface layer depth and plankton biomass distribution in the Arabian Sea. Deep-Sea Research 38, 531–553.

Brink, K., Arnone, R., Coble, P., Flagg, C., Jones, B., Kindle, J., Lee, C., Phinney, D., Wood, M., Yentsch, C., Young, D., 1998. Monsoons boost biological productivity in Arabian Sea. EOS 79, 165–169.

Burkill, P.H., Mantoura, R.F.C., Owens, N.J.P., 1993. Biogeochemical cycling in the northwestern Indian Ocean: a brief overview. Deep-Sea Research 40, 643–649.

Caron, D.A., Dennett, M.R., 2000. Phytoplankton growth and mortality during the 1995 Northeast Monsoon and Spring Intermonsoon in the Arabian Sea. Deep-Sea Research II, in press.

Cullen, J.J., Lewis, M.R., Davis, C.O., Barber, R.T., 1992. Photosynthetic characteristics and estimated growth rates indicate grazing is the proximate control of primary production in the Equatorial Pacific. Journal of Geophysical Research 97, 639–654.

Dickey, T., Marra, J., Sigurdson, D.E., Weller, R.A., Kinkade, C.S., Zedler, S.E., Wiggert, J.D., Langdon, C., 1998. Seasonal variability of bio-optical and physical properties in the Arabian Sea: October 1994–October 1995. Deep-Sea Research II 45, 2001–2025.

Dickey, T.D., Granata, T., Marra, J., Langdon, C., Wiggert, J., Chai, Z., Hamilton, M., Vasquez, J., Stramska, M., Bidigare, R., Siegel, D., 1993. Seasonal variability of bio-optical and physical properties in the Sargasso Sea. Journal of Geophysical Research 98, 865–898.

Dickey, T.D., Simpson, J.J., 1983. The influence of optical water type on the diurnal response of the upper ocean. Tellus 35, 142–154.

Dugdale, R.C., Goering, J.J., 1967. Uptake of new and regenerated forms of nitrogen in primary productivity. Limnology and Oceanography 12, 196–206.

Dugdale, R.C., Wilkerson, F.P., Minas, H.J., 1995. The role of a silicate pump in driving new production. Deep-Sea Research 42, 697–719.

Fasham, M., Ducklow, H., McKelvie, S., 1990. A nitrogen-based model of plankton dynamics in the oceanic mixed layer. Journal of Marine Research 48, 591–639.

Findlater, J., 1969. A major low-level air current near the Indian Ocean during the northern summer. Quarterly Journal of the Royal Meteorological Society 95, 362–380.

Fischer, A.S., 1997. Arabian Sea mixed layer deepening during the monsoon: observations and dynamics. Master's Thesis, MIT/WHOI, p. 130.

Gardner, W.D., Gumdersen, J.S., Richardson, M.J., Walsh, I.D., 1999. The role of seasonal and diel changes in mixed-layer depth on carbon and chlorophyll distributions in the Arabian Sea. Deep-Sea Research II 46, 1833–1858.

Haake, B., Ittekkot, V., Rixen, T., Ramaswamy, V., Nair, R.R., Curry, W.B., 1993. Seasonality and interannual variability of particle fluxes to the deep Arabian Sea. Deep-Sea Research 40, 1323–1344.

Kabanova, Y.G., 1968. Primary production of the northern part of the Indian Ocean. Oceanology 8, 214–225.

Kantha, L.H., Clayson, C.A., 1994. An improved mixed layer model for geophysical applications. Journal of Geophysical Research 99, 25235–25266.

Kiefer, D.A., 1993. Growth and light absorption in the marine diatom *Skeletonema Costatum*. In: Evans, G., Fasham, M. (Eds.), Towards a Model of Ocean Biogeochemical Processes. Springer, Berlin, pp. 93–122.

Kiefer, D.A., Kremer, J.N., 1981. Origins of vertical patterns of phytoplankton and nutrients in the temperate, open ocean: a stratigraphic hypothesis. Deep-Sea Research 28A, 1087–1105.

Kirk, J.T.O., 1983. Light and Photosynthesis in Aquatic Ecosystems. Cambridge University Press, Cambridge, p. 401.

Kumar, S.P., Prasad, T.G., 1999. Formation and spreading of Arabian Sea high-salinity water mass. Journal of Geophysical Research 104, 1455–1464.

Landry, M.R., Barber, R.T., Bidigare, R.R., Chai, F., Coale, K.H., Dam, H.G., Lewis, M.R., Lindley, S.T., McCarthy, J.J., Roman, M.R., Stoecker, D.K., Verity, P.G., White, J.R., 1997. Iron and grazing constraints on primary production in the central equatorial Pacific: an EqPac synthesis. Limnology and Oceanography 42, 405–418.

Large, W.G., McWilliams, J.C., Doney, S.C., 1994. Oceanic vertical mixing: a review and a model with a nonlocal boundary layer parameterization. Reviews of Geophysics 32, 363–403.

Madhupratap, M., Kumar, S.P., Bhattathiri, P.M.A., Kumar, M.D., Raghukumar, S., Nair, K.K.C., Ramaiah, N., 1996. Mechanism of the biological response to winter cooling in the northeastern Arabian Sea. Nature 384, 549–552.

Marra, J., Dickey, T.D., Ho, C., Kinkade, C.S., Sigurdson, D.E., Weller, R.A., Barber, R.T., 1998. Variability in primary production as observed from moored sensors in the central Arabian Sea in 1995. Deep-Sea Research II 45, 2253–2267.

Martin, J.H., Gordon, R.M., Fitzwater, S.F., 1991. The case for iron. Limnology and Oceanography 36, 1793–1803.

McCarthy, J.J., Garside, C., Nevins, J.L., 1999. Nitrogen dynamics during the Arabian Sea Northeast Monsoon. Deep-Sea Research II 46, 1623–1664.

McCreary, J.P. et. al., 2000. Effects of diurnal and intraseasonal forcing on mixed-layer and biological variability in the Arabian Sea. manuscript in preparation.

Measures, C.I., Vink, S., 1999. Seasonal variations in the distribution of Fe and Al in the surface waters of the Arabian Sea. Deep-Sea Research II 46, 1597–1622.

Mellor, G.L., Yamada, T., 1982. Development of a turbulence closure model for geophysical fluid problems. Reviews of Geophysics and Space Physics 20, 851–875.

Michaels, A.F., Knap, A.H., Dow, R.L., Gundersen, K., Johnson, R.J., Sorensen, J., Close, A., Knauer, G.A., Lohrenz, S.E., Asper, V.A., Tuel, M., Bidigare, R., 1994. Seasonal patterns of ocean biogeochemistry at the US JGOFS Bermuda Atlantic time–series study site. Deep-Sea Research 41, 1013–1038.

Morel, A., 1988. Optical modeling of the upper ocean in relation to its biogenous matter content (Case I waters). Journal of Geophysical Research 93, 10749–10768.

Morrison, J.M., Codispoti, L.A., Gaurin, S., Jones, B., Manghnani, V., Zheng, Z., 1998. Seasonal variation of hydrographic and nutrient fields during the US JGOFS Arabian Sea Process Study. Deep-Sea Research II 45, 2053–2101.

Nair, R.R., Ittekkot, V., Manganini, S.J., Ramaswamy, V., Haake, B., Degens, E.T., Desai, B.N., Honjo, S., 1989. Increased particle flux to the deep ocean related to the monsoons. Nature 338, 749–751.

Naqvi, S.W.A., Noronha, R.J., Shailaja, M.S., Somasundar, K., Sen Gupta, R., 1992. Some aspects of the nitrogen cycling in the Arabian Sea. In: Desai, B.N. (Ed.), Oceanography of the Indian Ocean. Oxford and IGH Publishing Co., Oxford, pp. 285–311.

Olson, R.J., SooHoo, J.B., Kiefer, D.A., 1980. Steady-state growth of the marine diatom *Thalassiosira pseudonana*: uncoupled kinetics of nitrate uptake and nitrite production. Plant Physiology 66, 383–389.

Rochford, D.J., 1964. Salinity maximas in the upper 1000 meters of the Indian Ocean. Australian Journal of Marine and Freshwater Research 15, 1–24.

Ruddick, B., 1997. Differential fluxes of heat and salt: implications for circulation and ecosystem modeling. Oceanography 10, 122–127.

Ryther, J.H., Hall, J.R., Pease, A.K., Bakun, A., Jones, M.M., 1966. Primary organic production in relation to the chemistry and hydrography of the western Indian Ocean. Limnology and Oceanography 11, 371–380.

Ryther, J.H., Menzel, D.W., 1965. On the production, composition, and distribution of organic matter in the Western Arabian Sea. Deep-Sea Research 12, 199–209.

Shetye, S.R., Gouveia, A.D., Shenoi, S.S.C., 1994. Circulation and water masses in the Arabian Sea, Proceedings of the Indian Academy of Sciences, Vol. 103, Lotus Printers, New Delhi, India.

Smith, S.L., Codispoti, L.A., Morrison, J.M., Barber, R.T., 1998. The 1994–1996 Arabian Sea Expedition: an integrated, interdisciplinary investigation of the response of the northwestern Indian Ocean to monsoonal forcing. Deep-Sea Research II 45, 1905–1915.

Tomczak, M., Godfrey, J.S., 1994. Regional Oceanography: an introduction. Pergammon, London, p. 422.

Warren, B.A., 1994. Context of the suboxic layer in the Arabian Sea. Proceedings of the Indian Academy of Sciences, Vol. 103, Lotus Printers, New Delhi, India.

Weller, R.A., Baumgartner, M.F., Josey, S.A., Fischer, A.S., Kindle, J.C., 1998. Atmospheric forcing in the Arabian Sea during 1994–1995: observations and comparisons with climatology and models. Deep-Sea Research II 45, 1961–1999.

Wiggert, J., 1995. Analysis of High Resolution Physical/Bio–optical Moored Time Series and Comparison to a 1-D Interdisciplinary Ocean Model, Ph.D. Thesis, University of Southern California, p. 263.

Wroblewski, J., 1977. A model of phytoplankton plume formation during variable Oregon upwelling. Journal of Marine Research 35, 357–394.